Modeling *S* wave amplitude patterns for events in the Kurile slab using three-dimensional Gaussian beams

Kris L. Pankow[1] and Thorne Lay

Center for the Study of Imaging and Dynamics of the Earth, Institute of Geophysics and Planetary Physics and Earth Sciences Department, University of California, Santa Cruz, California, USA

Received 25 April 2001; revised 17 December 2001; accepted 22 December 2001; published 22 August 2002.

[1] The shear velocity structure of the subducted Kurile slab is modeled using shear wave amplitude residual spheres. We measure long-period *SH* and *ScSH* phase amplitudes for 10 intermediate and deep focus earthquakes recorded at World-Wide Standardized Seismograph Network and Canadian Seismic Network stations from 1967 to 1986. After correction for source radiation pattern, geometric spreading, and empirical receiver/upper mantle effects, the data for intermediate depth Kurile slab events show smoothly varying amplitude residual sphere patterns with low amplitudes concentrated in the direction down the slab dip. The data are modeled using three-dimensional dynamic ray tracing and a three-dimensional Gaussian beam method. Starting models are taken from previous *P* and *S* wave arrival time residual sphere studies. Three-dimensional ray tracing indicates that ray patterns and resulting amplitudes are very sensitive to the depth extent of the slab and to the position of the event relative to the across-slab velocity gradient. This sensitivity allows us to place some constraints on the Kurile slab geometry, position of each event within the slab, and penetration depth of coherent slab structure. Our final slab model is defined by an asymmetric error function that peaks at 4% higher velocity than Preliminary Reference Earthquake Model 25 km from the top of the slab. The total width of the thermal anomaly averages 140 km. The slab is tabular and extends to 670 km in the northern half of the Kurile subduction zone. In the southern half of the subduction zone the slab flattens along the 670 km discontinuity and deflects laterally, persisting to 750 km depth. *INDEX TERMS:* 7203 Seismology: Body wave propagation; 7207 Seismology: Core and mantle; 8120 Tectonophysics: Dynamics of lithosphere and mantle—general; *KEYWORDS:* slab structure, Gaussian beams, mantle convection, residual spheres, *S* wave amplitudes

1. Introduction

[2] The depth to which subducting oceanic slabs penetrate is a critical aspect of the convective style of the mantle [e.g., *Silver et al.*, 1988; *Lay*, 1994, 1997; *Olson et al.*, 1990; *Jordan et al.*, 1989]. If slabs penetrate to well below the 670-km discontinuity, there must be significant mixing of upper and lower mantle material, possibly involving whole mantle convection. If slabs are unable to significantly penetrate into the lower mantle, layered convection is likely, and the lower mantle may be distinct from the upper mantle in its bulk chemistry. Recognizing that the 670-km discontinuity does appear to resist slab penetration, presumably due to the negative Clapeyron slope of the associated phase transition of $(Mg,Fe)_2SiO_4$ in spinel structure to (Mg,Fe)-SiO_3 in perovskite structure plus (Mg,Fe)O, intermediate models in which some slabs do penetrate and others do not have been proposed, with thermal inertia of the slabs playing a critical role [e.g., *Silver et al.*, 1988]. Seismological methods, which can image three-dimensional seismic velocity structures in the mantle, are particularly promising for resolving the extent of slab penetration and the associated affects on the sinking material. Characterizing the convective style of mantle downwellings is essential to understanding the dynamics and thermal evolution of the planet.

[3] For several decades, studies of *P* wave arrival time residuals have addressed the above question by seeking to image the velocity structure of subducting slabs. There has been great progress, and in many cases, images of cold, relatively high seismic velocity material encompassing deep earthquake activity or extending below it have been extracted [cf. *van der Hilst et al.*, 1998; *Lay*, 1994]. However, the details of deep slab structure are still much in question, and there have been contradictory results for some subduction zones. For instance, in the Kurile Islands subduction zone, it has been postulated on the basis of *P* wave arrival time residual spheres that the slab is tabular and penetrates essentially undeformed (possibly with some advective thickening) to at least 1200 km depth [*Jordan*, 1977; *Creager and Jordan*, 1984, 1986; *Fischer et al.*, 1988], while a different *P* wave arrival time residual sphere study designed to better suppress lower mantle contributions images a Kurile slab for which the morphology varies

[1]Now at Seismograph Stations, University of Utah, Salt Lake City, Utah, USA.

0148-0227/02/2001JB000594$09.00

from a very wide structure that penetrates to at least 1200 km in the north to a slab that is deflected along the 670-km discontinuity in the south [*Ding and Grand*, 1994]. This variable morphology is supported to a certain degree by tomographic studies of the same region [*van der Hilst et al.*, 1991, 1993, 1997; *Fukao et al.*, 1992]. However, tomography studies that include a priori information about the upper mantle slab geometry favor short narrow slabs [*Zhao et al.*, 1994; *Deal and Nolet*, 1999] and, in most cases, full nonlinear iterative tomography which accounts for ray bending and event relocation in the heterogeneous model has not been performed. An *S* wave arrival time residual sphere study [*Pankow and Lay*, 1999] does not resolve any flattening of the slab in the southern part of the zone and is not able to distinguish between a widened or a tabular model, but their models suggest that relatively weak slab velocity anomalies may penetrate to 800 km depth. The details of slab dip and velocity anomaly also vary from model to model, although some researchers focus on common features shared by some models.

[4] Much of the ambiguity in the current generation of slab models appears to reflect the inadequacies of using only *P* or *S* wave arrival times. Although arrival times are relatively easy to obtain, especially *P* wave bulletin times, there are two factors that significantly affect arrival time studies. The first is that it is difficult to isolate the near-source contribution to the total travel time [e.g., *Schwartz et al.*, 1991a, 1991b; *Gaherty et al.*, 1991; *Ding and Grand*, 1994; *Suetsugu*, 1999; *Pankow and Lay*, 1999]. Arrival time anomalies arise from integration along the entire path through the heterogeneous interior, and the contribution from the near-source path in the slab may be only a small part of the overall anomaly. While early studies relied only on azimuthally averaged station corrections or very low resolution aspherical Earth models in order to make corrections, the two main strategies that have been used more recently to isolate the near-source contributions involve empirical path corrections and differential residual spheres. Empirical path corrections [e.g., *Zhou and Anderson*, 1989; *Gaherty et al.*, 1991; *Pankow and Lay*, 1999; *Suetsugu*, 1999] are formed by using events and phases from regions close to the study area so that the deep mantle and near-receiver contributions to the anomaly on each path to a distant station are similar to those for events in the deep slab. While these corrections remove distant path effects, they may also remove part of the near-source signal, as the nearby seismic regions intrinsically tend to be in or near slab structures. Differential residual spheres [e.g., *Ding and Grand*, 1994; *Pankow and Lay*, 1999] take advantage of the fact that nearby events have similar paths away from the source region; by differencing the residuals at common stations for the two events and projecting out any relative location term, one is left with differential near-source contributions. While this technique removes distant path effects, the resulting residual is difficult to interpret because the slab model needs to be accurate for both events, not just for one, and there is a tendency to lose information about slab absolute velocity anomalies.

[5] The second factor that significantly affects travel time studies is the need to locate the event in order to turn arrival times into travel time estimates and their associated anomalies with respect to a reference model. Using standard radially symmetric reference models, intermediate and deep earthquakes are often mislocated in an absolute sense by 10 km or more laterally and in-depth [*Engdahl et al.*, 1998]. Lack of knowledge of the true structure means that the source locations and origin times for slab events are always just estimates for a given model. The location process effectively extracts any degree 1 term from the data [*Jordan*, 1977]; thus any systematic degree 1 contributions arising from aspherical structure are mapped into erroneous location parameters, and one is dependent on higher-order structure to back out the original structure by an iterative nonlinear modeling approach. Typically, the necessary process of estimating a location for the event is expected to suppress most of the slab-related travel time anomaly present in teleseismic observations of intermediate and deep focus events, and many ''artificial'' residual patterns are introduced by the location process that must be simulated in the model processing to avoid misinterpretation [*Creager and Boyd*, 1992; *Lay*, 1997]. *Pankow and Lay* [1999] showed that the location affect on model travel time residual spheres produced for a tabular slab made it extremely difficult to resolve the thickness of the slab. *Koper et al.* [1998] further demonstrated the difficulty of resolving internal slab structure with travel times.

[6] These two factors affecting arrival time studies make the results of different analyses quite dependent on the specific data treatment and modeling process. While there are undoubtedly some consistencies in the images from different studies, the discrepancies remain very significant, weakening any inferences about dynamical processes.

[7] Given the limitations of arrival time studies and the advances in computer technology, it is reasonable to consider other aspects of seismic wave trains that may constrain slab structure. Previous work on waveform effects generated by the slab include study of high-frequency precursors [*Ansell and Gubbins*, 1986; *Gubbins and Snieder*, 1991; *van der Hilst and Snieder*, 1996], two-dimensional downdip amplitude anomalies [*Cormier*, 1989; *Vidale*, 1987; *Weber*, 1990; *Gaherty et al.*, 1991; *Suetsugu*, 1989, 1999], and distortion of teleseismic signal pulse shapes [*Silver and Chan*, 1986; *Beck and Lay*, 1986; *Schwartz et al.*, 1991a; *Cormier*, 1989; *Vidale*, 1987]. In fact, theoretical studies have shown that the best discriminants between many slab models involve waveform and amplitude characteristics rather than travel times [*Cormier*, 1989; *Vidale*, 1987; *Weber*, 1990; *Koper et al.*, 1998]. However; there have as yet been only a few amplitude investigations of deep slab structure, despite many early investigations of defocusing effects by slabs for nuclear tests in the Aleutians [e.g., *Sleep*, 1973] (and see the review by *Lay* [1997]). This is in part due to the difficulty of generating teleseismic waveforms for realistic three-dimensional slab structures. Existing algorithms for making such calculations are expensive and limited in accuracy due to the relatively large (4–10%) slab velocity anomalies involved and the dipping structure, which produces complex patterns of caustics and diffractions. Most previous studies used two-dimensional algorithms: finite difference, finite element, or Gaussian beams. With a two-dimensional algorithm one is restricted to looking at stations in the downdip direction, and typically, the range of takeoff angles available is quite small (e.g., *PcP* phases are usually not large enough to measure reliably).

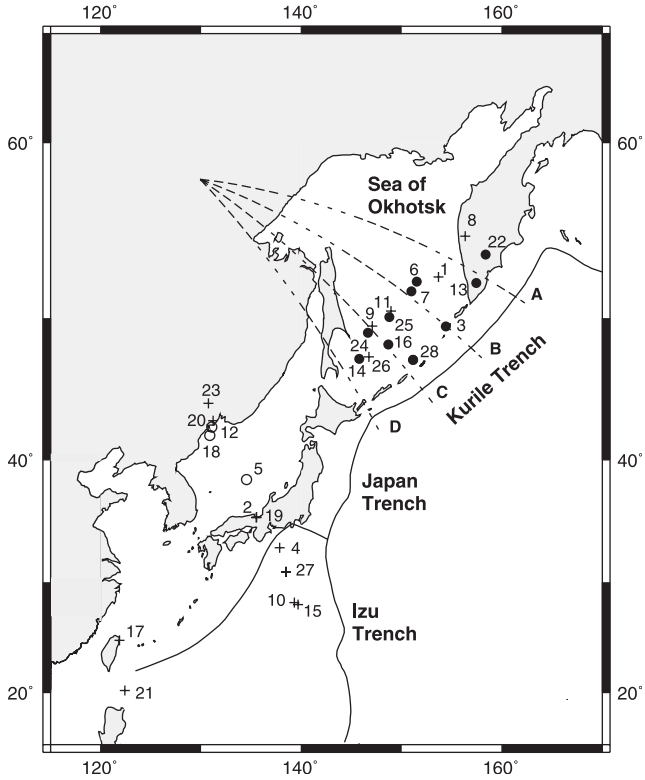

Figure 1. Mercator projection of the northwestern Pacific region. Solid circles indicate epicenters for the 10 events with complete *S* wave coverage used in the amplitude modeling. The three open circles indicate epicenters for events with complete *S* wave coverage that were not used in the modeling. Crosses indicate event epicenters for additional events with azimuthally limited data that were measured by *Gaherty et al.* [1991] and are used with the other events to calculate station statics. The event numbers correspond to Table 1. The dashed lines correspond to cross sections for the model determined in this study. They are shown in Figure 12.

There is much more information in the full range of azimuths, especially along slab strike where ray paths are strongly refracted by the slab velocity gradients [*Silver and Chan*, 1986]. There have been a few studies using three-dimensional Gaussian beams. *Sekiguchi* [1992] examined three-dimensional effects for local distances, essentially up the dip of the slab, while *Cormier* [1989] considered three-dimensional effects for teleseismic distances. In both cases, several tests were run to predict waveform effects given different model parameters, and to a very limited extent the approach was applied to data.

[8] We apply three-dimensional dynamic ray tracing and a Gaussian beam method to interpret the first systematically processed set of *S* wave amplitude residual spheres for a deep slab of which we are aware. Our events are located in the Kurile slab, which has the most favorable azimuthal coverage by teleseismic observations of any circum-Pacific slab. Amplitude residual spheres require important corrections for source radiation pattern and deep path and receiver contributions, but their processing does not involve significant artifacts associated with the location process. We analyze long-period transversely polarized shear wave observations from 10 intermediate and deep events, first establishing that the data have some systematic amplitude patterns that appear to be isolated as near-source effects. Distinct from arrival time studies, the amplitude patterns prove very sensitive to position of the source within the slab velocity anomaly and to velocity gradients and absolute velocities. We seek to resolve aspects of the Kurile slab based on the fit of focusing and defocusing patterns seen in the data, limited by the stability of the ray-based method, which breaks down in strong shadow zones at some azimuths for almost all slab models. While this precludes comprehensive quantitative modeling, the general patterns and behavior of the amplitude observations can be matched qualitatively.

2. Data Analysis

[9] Baseline-to-peak amplitudes were measured for transversely polarized *S*, *ScS*, *sS*, and *sScS* phases (when possible) from 28 intermediate to deep focus earthquakes in northwestern Pacific subduction zones (Figure 1 and Table 1). The data are all long-period shear waves recorded by the World-Wide Standardized Seismic Network (WWSSN) and the Canadian Seismograph Network (CSN) at distances between 35° and 90°. The events occurred between 1964 and 1986 and range in magnitude from m_b 5.5 to 6.1. Events were selected based on favorable signal-to-noise ratios and simple *SH* waveforms. The horizontal components at each station were digitized and rotated to obtain the transverse and radial components, and all traces were corrected to a gain of 1500 prior to measuring. For 10 of the events in the Kurile slab we obtained particularly complete coverage to be used in the modeling. All 28 events are used to calculate station/deep path statics. Broadband digital recordings are now accumulating rapidly, but the stations involved differ and the number of suitable deep Kurile events is still relatively small, so we restrict this exploratory investigation to the large archive of older analog data.

[10] Long-period waves (5–15 s predominant periods) are expected to have reduced sensitivity to narrow slab structures compared to short-period arrivals [*Weber*, 1990] but have the key advantage of being coherent, enabling systematic amplitude measurements to be made. Long-period *S* waves are also much less affected by attenuation variations than short-period *S* waves, so much more complete sampling is attainable from the global analog networks. This should make it more straightforward to model the data and to detect any near-source systematic contributions. The depth and core phases were included to extend the range of takeoff angles. At most azimuths the depth phases quickly exit the slab, and they should provide very different sampling of any slab structure than the direct downgoing phases, although they may encounter complex velocity structure in the wedge above the slab. *ScS* phases thoroughly sample steeply dipping slab structure, which proves important in the Kurile slab, and unlike *PcP*, the shear waves reflected from the core have large amplitudes. The logarithm (base 10) of each amplitude deviation with respect to the mean for the 10 well-sampled events are plotted on residual spheres [*Davies and McKenzie*, 1969] in Figure 2(left). The raw data show coherent slowly varying

Table 1. Event Information[a]

Event	Date	Origin Time, UT	Location			Source	Focal Mechnism			Reference
			Latitude, °N	Longitude, °E	Depth, km		φ	δ	λ	
1	18 March 1964	0437:25.7	52.56	153.67	424	ISC	48	84	−76	L83
2	13 Aug. 1967	2006:52.3	35.43	135.49	367	ISC	238	68	−84	G91
3	1 Dec. 1967	1357:05.0	49.46	154.44	143	E	56	97	109	ts
4	28 Feb. 1968	1208:01.8	32.95	137.85	348	ISC	180	86	97	M71
5	31 March 1969	1925:28.4	38.42	134.60	404	E	31	80	225	ts
6	5 Sept. 1970	0752:29.6	52.16	151.46	583	E	1	73	−90	ts
7	29 Jan. 1971	2158:06.2	51.60	150.95	544	E	35	72	−113	ts
8	27 May 1972	0406:49.6	54.97	156.33	397	ISC	24	85	−94	G91
9	21 Aug. 1972	0623:48.6	49.47	147.08	573	ISC	15	17	47	G91
10	31 Jan. 1973	2055:54.2	28.22	139.30	508	ISC	317	72	−74	G91
11	28 July 1973	2006:35.4	50.45	148.92	585	ISC	51	76	−107	L83
12	10 Sept. 1973	0743:33.9	42.42	131.11	564	E	21	16	110	ts
13	21 Sept. 1974	1555:08.9	52.16	157.95	121	E	206	78	85	ts
14	10 July 1976	1137:16.4	47.28	145.79	415	E	49	82	−117	ts
15	12 Dec. 1976	0118:51.1	28.04	139.67	503	ISC	328	72	−74	G91
16	21 June 1978	1110:42.0	48.21	148.63	404	E	289	41	35	ts
17	2 Sept. 1978	0157:34.2	24.81	121.87	115	ISC	34	28	138	G91
18	16 Aug. 1979	2131:26.8	41.78	131.07	586	E	57	33	136	ts
19	31 March 1980	0732:32.4	35.49	135.52	362	ISC	214	44	−149	G91
20	27 Nov. 1981	1721:44.3	42.93	131.19	525	ISC	66	25	175	CMT
21	3 July 1983	0249:28.2	20.19	122.41	221	ISC	332	37	−83	CMT
22	24 July 1983	2307:32.5	53.89	158.42	183	E	317	5	0	ts
23	8 Oct. 1983	0745:26.3	44.21	130.74	551	ISC	349	29	88	G91
24	1 Feb. 1984	0728:30.4	48.93	146.59	585	E	231	81	82	ts
25	20 April 1984	0631:12.03	50.00	148.76	590	E	252	18	−73	ts
26	23 April 1984	2140:34.2	47.44	146.73	399	ISC	18	40	110	G91
27	24 April 1984	0411:28.5	30.89	138.48	398	ISC	86	36	−150	G91
28	19 July 1986	0559:38.8	47.18	151.10	154	E	31	74	−68	ts

[a] ISC locations taken from ISC Bulletin; E locations provided by E. R. Engdahl (personal communication, 1998). Focal mechanism references: L83, *Lay* [1983]; M71, *Mikumo* [1971]; G91, *Gaherty et al.* [1991]; CMT, Harvard centroid moment tensor catalogue; ts, this study.

patterns that indicate combined contributions from source radiation pattern and other effects. Note that the focal sphere coverage is quite good, comparable to that obtained in previous arrival time studies for both *P* and *S* waves for Kurile sources [e.g., *Creager and Jordan*, 1986; *Pankow and Lay*, 1999]. In order to isolate any near-source propagation effects we must remove other sources of amplitude variation.

2.1. Equalized Amplitudes

[11] We equalize the observed amplitudes to an isotropic source and a uniform propagation distance for a laterally uniform Earth model. This is done by making corrections for (1) geometric spreading for each phase type (calculated by ray tracing for the preliminary reference Earth model (PREM) of *Dziewonski and Anderson* [1981]), (2) differential attenuation in the PREM attenuation structure, and (3) source *SH* radiation pattern for double-couple models. We do not consider anisotropic corrections, as lithospheric anisotropy below the receivers is expected to have small effect on our relatively long-period signals. The geometric spreading corrections are straightforward, and the differential attenuation corrections are quite small for the separate upgoing and downgoing data populations. The more significant radiation pattern correction is optimized by inverting for the double-couple focal mechanism most consistent with the observed long-period *S* waves. We use a damped iterative least squares inversion [*Gaherty et al.*, 1991]. The *SH* and *ScSH* amplitude observations (corrected for attenuation and geometric spreading) are combined with a few *SH*/*SV* amplitude ratios (to stabilize the inversion) and are iteratively inverted for perturbations to the strike, dip, and rake of published *P* wave first-motion mechanisms or other starting mechanisms. Our final double-couple focal mechanisms are listed in Table 1, and the starting and final *P* and *SH* radiation pattern nodes are shown in Figure 3.

[12] Typically, we find only a few degrees change in mechanism relative to the starting *P* wave first-motion mechanism. This is a very important point, as the radiation pattern corrections are the largest corrections made, and they involve slowly varying patterns that may trade off with slab focusing effects. While the adjustments of the source mechanism prove to be small, we feel that they are worthwhile, given that first motions of high-frequency *P* waves may not adequately represent the fault geometry affecting the 10-s period *S* wave radiation from the source, along with the fact that we desire for our *S* wave amplitude data to be as free as possible of source mechanism effects before modeling slab effects. Of course, rupture directivity effects and interference between subevents may not be adequately represented by point source double-couple solutions. We rely on the relatively long-period (10 s) of the *S* observations, and the modest size of our events to mitigate the latter effects, but concern about the focal mechanisms remains.

[13] Inaccurate focal mechanism estimates may result from poor station coverage, source rupture complexity, or unaccounted for modulations of observed waveform amplitudes and ray path deflections produced by the very slab structure that we seek to model. The main concern is that slab effects may be projected into false radiation pattern corrections and resulting false trends in the ''corrected'' data may be mapped into incorrect slab structures. Such tradeoffs between source parameters and structure are analogous to those plaguing travel time investigations of slabs. Figure 4

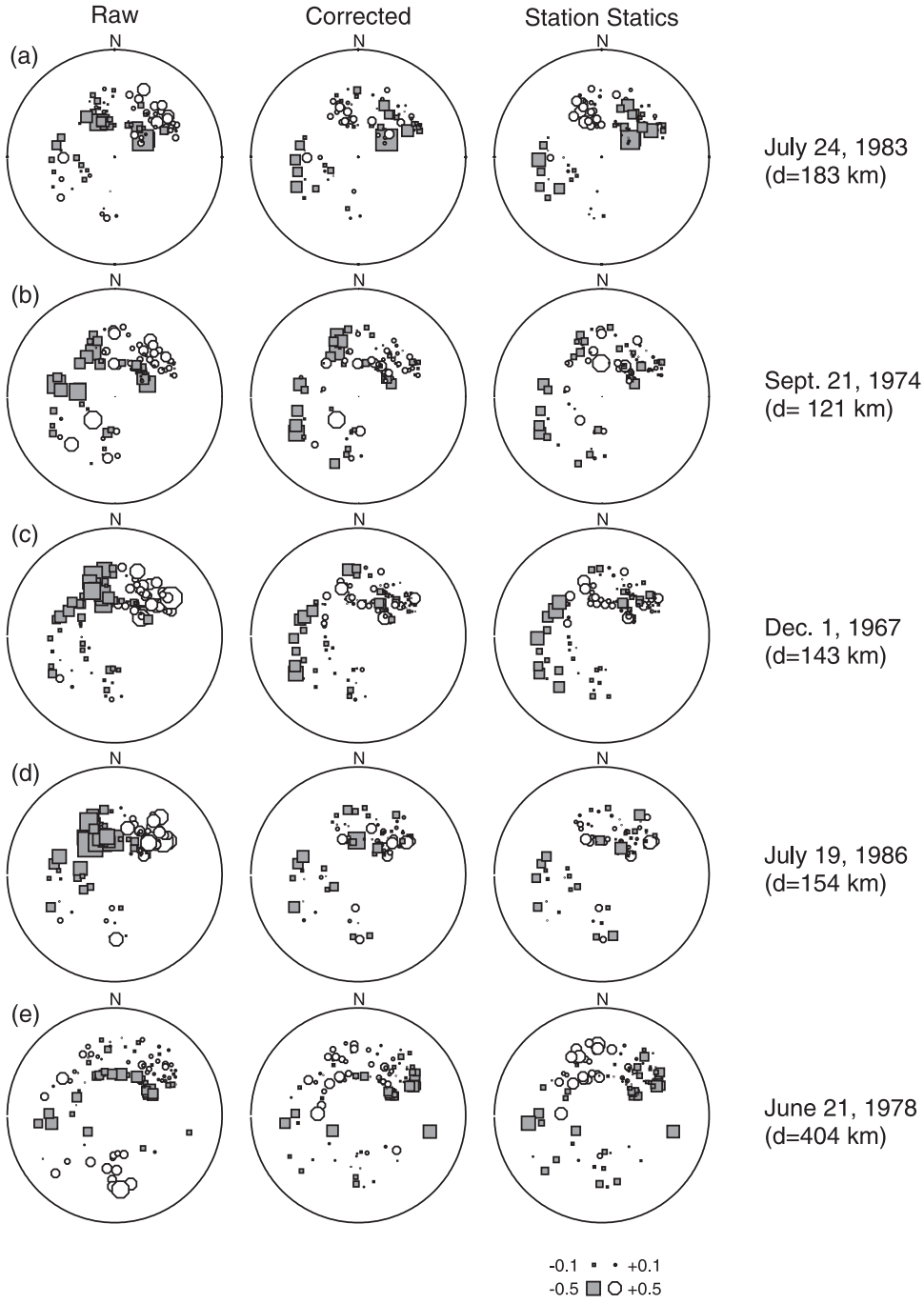

Figure 2. (left) Raw amplitudes, (middle) amplitudes corrected for geometric spreading, attenuation, and radiation pattern, and (right) amplitudes further corrected for station statics for the 10 well-sampled events are plotted on amplitude residual spheres. The squares are smaller than average amplitudes, the circles are larger than average amplitudes, and the crosses (positive) and pluses (negative) are residuals that are less than ±0.1. The takeoff angle corresponding to the circumference of the circle is 60°. The *ScS* values plot in the inner ring of each projection, and the outer ring is *S* values. The log (base 10) of each amplitude has been taken and the mean for each residual sphere is removed before plotting.

demonstrates the potential effects of such trade-offs for the *S* wave amplitude data. Figure 4a shows a *P* wave radiation pattern (solid line) used to compute theoretical *SH* amplitudes for a realistic data sampling corresponding to the event of 1 December 1967 (Figure 4b). The logarithmic *SH* amplitude pattern, with symbols that retain the polarity, is shown in Figure 4c; note that large symbols correspond to low amplitudes. Ray tracing through a simple tabular slab model extending deeply below the 143-km source depth is performed for the associated fault mechanism, giving total (logarithmic) amplitudes shown in Figure 4d, again retaining the sense of polarity. The isolated propagation term, showing

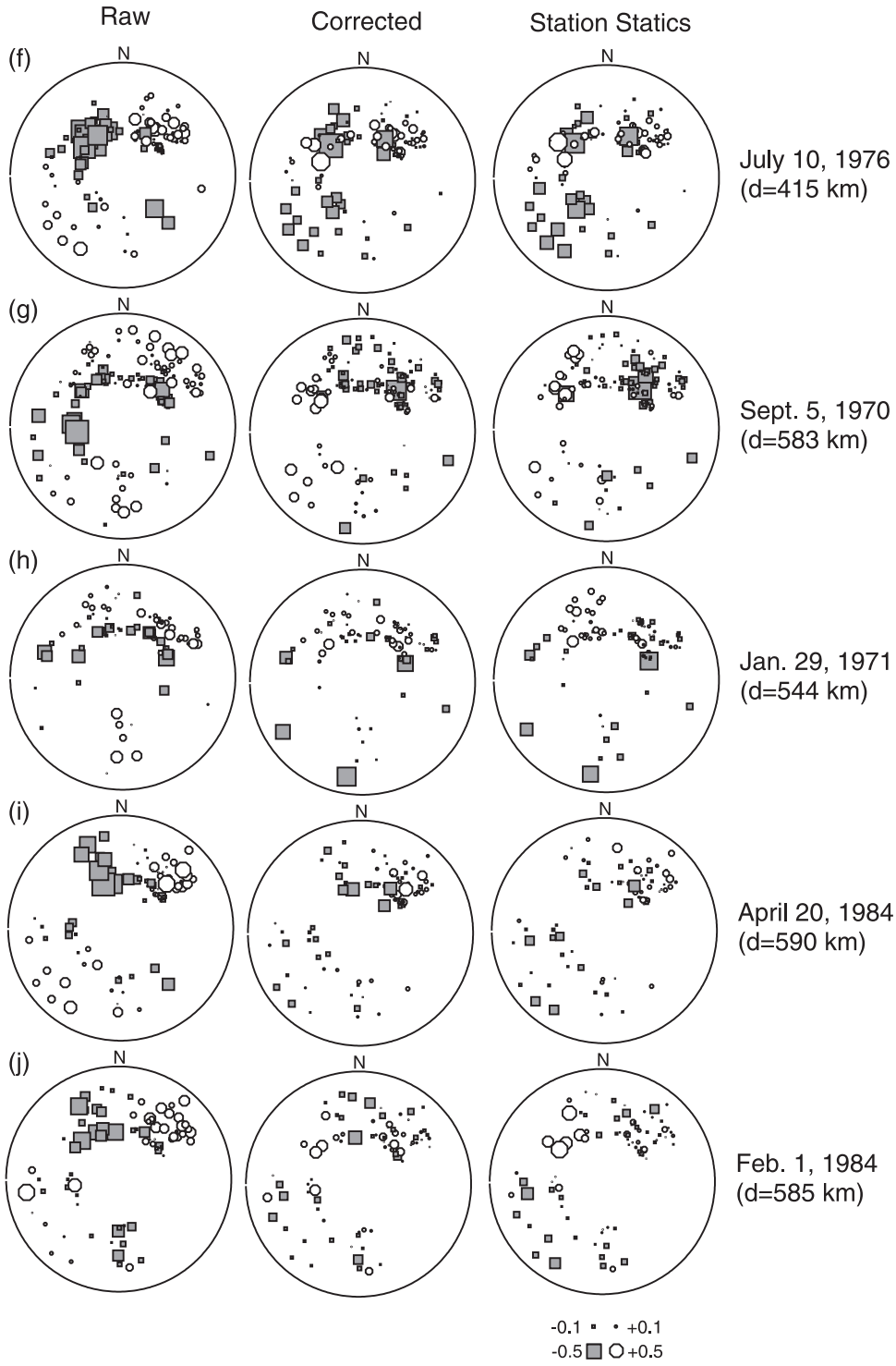

Figure 2. (continued)

strong downdip defocusing toward the northwest, is shown in Figure 4e. If the amplitudes in Figure 4d are inverted for the best focal mechanism, the result is the incorrect mechanism (dashed line) shown in Figure 4a. Application of corrections for the incorrect focal mechanism leads to biased anomalies shown in Figure 4f; modeling of these would result in an inaccurate slab model, although the basic downdip defocusing is not fully absorbed into the radiation pattern correction. Slab effects may certainly bias the *P* wave first-motion mechanism as well; however, it is unlikely that this will be in the same manner as for *S* wave amplitudes.

[14] We rely on the facts that we find very small changes relative to the *P* wave starting solutions and that we have substantial variation in *SH* radiation patterns (Figure 3) to proceed with modeling the corrected patterns for slab anomalies. Stations near *SH* radiation nodes are removed from the data set since they have large, potentially inaccurate correction factors. The amplitude anomalies with

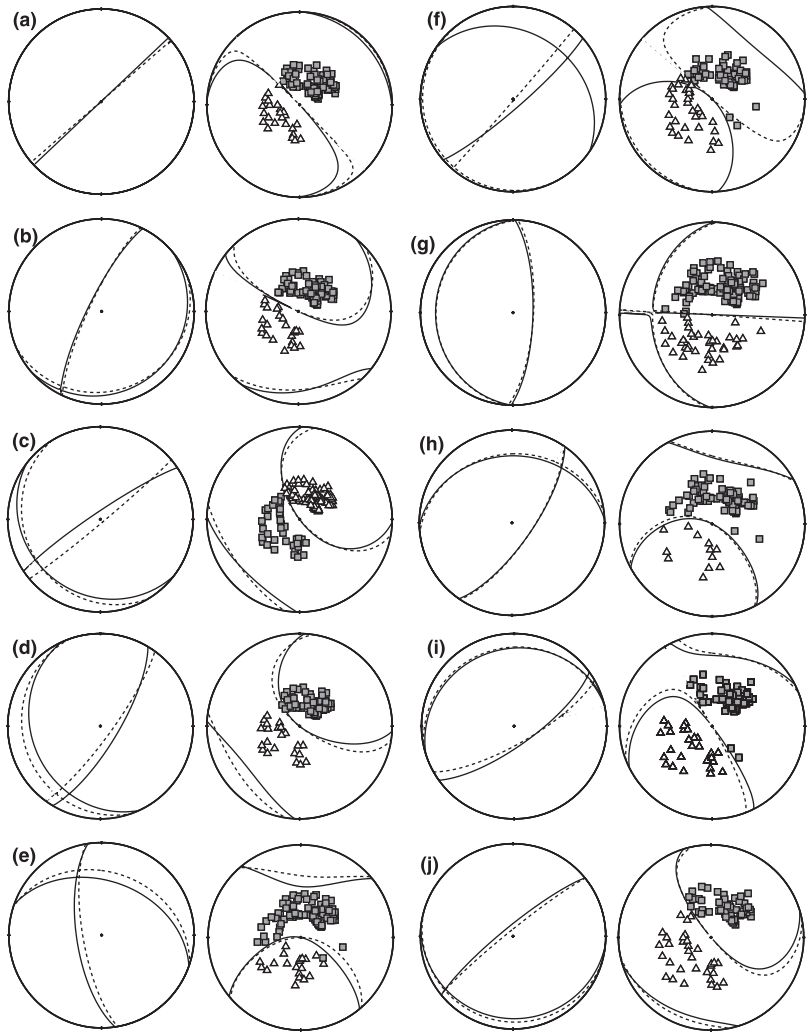

Figure 3. Each pair of lower hemisphere focal spheres shows on the left the *P* wave nodal planes for the starting mechanism used in each amplitude inversion (dashed line), and the final solution (solid line), and on the right, the distribution of *SH* amplitude observations (symbols indicate polarity) and the *SH* radiation nodes for the starting (dashed line) and final (solid line) solutions. (a) 24 July 1983, (b) 21 September 1974, (c) 1 December 1967, (d) 19 July 1986, (e) 21 June 1978, (f) 10 July 1976, (g) 5 September 1970, (h) 1 January 1971, (i) 20 April 1984, and (j) 1 February 1984.

respect to the mean value, corrected to an isotropic source at a uniform propagation distance are shown in Figure 2 (middle). The corrected patterns are significantly different from the raw observations, mainly due to the radiation pattern correction. For example, the event of 24 July 1983 has reversals in sign of anomalies in the northwest and southwest quadrants. The large effect indicates the critical importance of accurate radiation pattern. For some events, such as 1 December 1967, 19 July 1986, 20 April 1984, and 1 February 1984, observed low amplitudes toward the northwest are largely accounted for by radiation pattern corrections, although this is the region where strong slab defocusing might be expected. Some loss of slab anomaly, like that demonstrated in the experiment in Figure 4, could be occurring. However, there are significant features in common between events in different depth bands that suggest that the corrections are revealing a shared near-source effect. Note that the four events shallower than 200 km depth all have a band of relatively low amplitudes dipping toward the west, which is plausibly associated with defocusing by a high-velocity slab. This feature is not as evident in the raw residuals. The strength of amplitude fluctuations is comparable between these events and is similar to that for the distinct patterns seen in the two events near 400 km depth. It is very interesting to note that the four events deeper than 400 km depth show both less coherent clustering of anomalies and reduced overall fluctuations (except for intermittent large-amplitude outliers). This suggests that there is a fundamental difference in the slab-induced amplitude signal for intermediate depth events relative to that for very deep events in this arc. It is apparent that somewhat different patterns emerge as a function of depth, but nonetheless, we must be concerned about systematic amplitude anomalies for observations at a given station, with lateral variations in upper mantle attenuation, long-term errors in instrument calibration, and/or receiver and

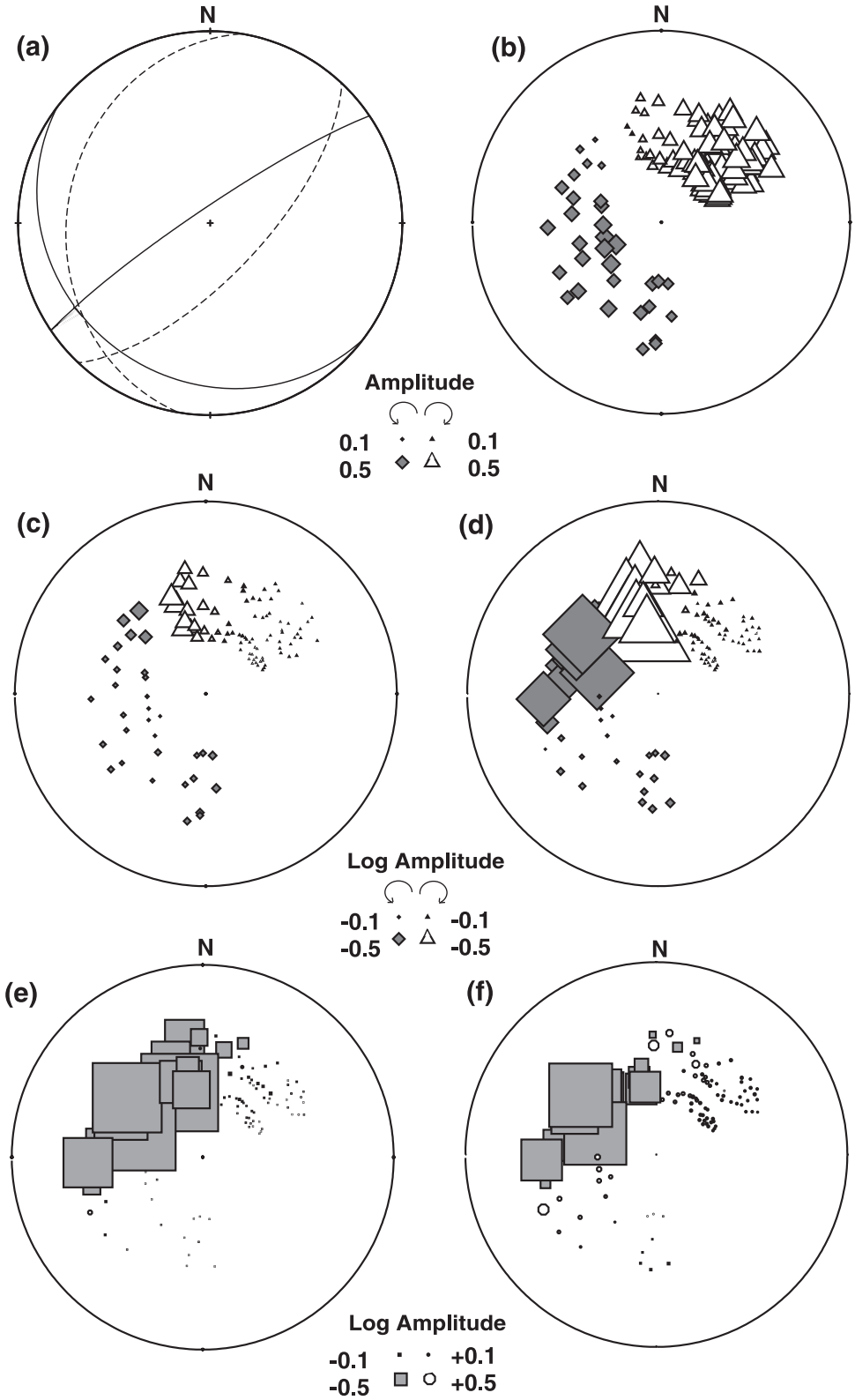
N
(a)
N
(b)
Amplitude
0.1
0.5
0.1
0.5
N
(c)
N
(d)
Log Amplitude
-0.1
-0.5
-0.1
-0.5
N
(e)
N
(f)
Log Amplitude
-0.1
-0.5
+0.1
+0.5

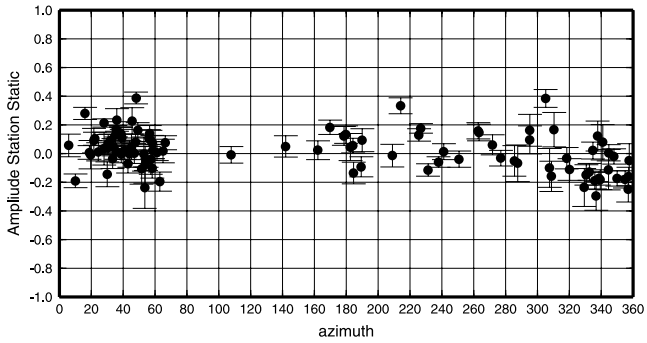

Figure 5. Empirical station/path corrections calculated from events located in northwest Pacific subduction zones. The error bars are the standard error of the mean. Corrections based on fewer than five measurements or standard errors of the mean larger than 0.15 are omitted.

upper mantle focusing effects. We attempt to account for this possibility next.

2.2. Path Specific Corrections

[15] Given that travel time residuals have significant contributions from distant path effects [*Pankow and Lay*, 1999; *Ding and Grand*, 1994; *Gaherty et al.*, 1991; *Schwartz et al.*, 1991a, 1991b; *Zhou et al.*, 1990], we anticipate that individual path effects beneath the receivers and in the deep mantle will contribute to the amplitude residuals. In order to correct for this contribution we empirically determine a set of amplitude station corrections for our data. The station correction terms were calculated using a least squares inversion that minimized the scatter in the radiation pattern-corrected amplitude residuals at each station for all 28 northwest Pacific subduction zone events [*Gaherty et al.*, 1991; *Pankow and Lay*, 1999]. Data for each phase (*S*, *ScS*, *sS*, *sScS*) were treated as though they were from distinct events, giving a total of 100 "pseudoevents." A total of 2656 measurements were used in the inversion. For our final corrections we remove any station with less than five observations and any station whose standard error of the mean for the correction term is larger than 0.15. The resulting statics, which involve some ray parameter averaging but are appropriate receiver crustal and upper mantle corrections for the azimuth to the Kurile source region, are quite well constrained (Figure 5).

[16] Figure 2(right) shows the results of application of these station/upper mantle correction terms to the amplitude residuals. The major danger of using empirically derived statics is the potential for projecting systematic near-source contributions into the receivers due to similarity of slab geometry relative to the stations for the northwestern Pacific subduction zones. However, comparing Figures 2(middle) and 2(right), it does not appear that significant coherent signal is projected away. The effect of applying the station terms is to actually accentuate some of the patterns seen in Figure 2(middle), while reducing some of the scatter. Ideally, separate corrections would be made for *S* and *ScS* phases to allow for the possibility of systematic ray parameter dependent trends, as was done for travel times by *Pankow and Lay* [1999], but our calibration data set does not have sufficient sampling to enable this. Thus the possibility remains that there are still contributions from differential effects of lower mantle structure on *S* and *ScS* amplitudes, but future efforts with larger data sets will be required to address this possibility.

2.3. Final Amplitude Residual Spheres

[17] After making the various corrections described above, we have our final set of *SH* wave amplitude residual spheres, with patterns of focusing (positive residuals, circles) and defocusing (negative residuals, solid squares) relative to the mean value. These are the first *S* wave amplitude residual spheres with complete azimuthal coverage for a large number of slab events of which we are aware. Coherent spatial patterns are still most prominent for the events <200 km in depth, with low amplitudes in a westward to northwest dipping band and some focusing on paths steeply dipping toward the north. In the northeast quadrant, there are significant amplitude variations, but these are not very coherent from event to event, suggesting that these arise from sensitive along-slab strike focusing and defocusing. While there is some rapidly varying scatter superimposed on the data at all azimuths, it appears that a long-wavelength component of near-source contribution has been isolated in the corrected data. The scatter, which is quite large, is undoubtedly enhanced by the variable calibration of the WWSSN data and the errors in digitization and rotation of the seismograms. This leads us away from focusing on isolated large anomalies.

[18] The patterns are quite different for the two events near 400 km depth. The event of 21 June 1978 (event 16 in Table 1 and Figure 1, depth of 404 km) shows a smooth pattern dominated by focusing downdip over a broader range than for any of the shallower events. The event of 10 July 1976 (event 14, depth of 415 km) exhibits a broad swath of lower amplitudes as might be expected for a more steeply dipping slab near this source. The change in the pattern suggests either a change in slab structure or in event positioning within the slab below 400 km. Events at >500 km depth have very

Figure 4. (opposite) Demonstration of the possible bias of radiation pattern corrections by slab propagation effects. (a) *P* wave radiation nodes for a starting focal mechanism (solid line) and for a biased solution obtained by inverting *S* amplitudes contaminated by slab effects (dashed line). (b) *SH* amplitudes plotted in a lower hemisphere projection for the starting mechanism. (c) Logarithm of the *SH* amplitudes in Figure 4b, where the symbols indicate polarity. (d) Logarithm of the *SH* amplitudes for the starting mechanism after propagation through a tabular slab model. The source is placed at 143 km depth in the slab structure and the amplitudes are computed with radiation pattern and propagation effects included. These "data" are then inverted to give the biased focal mechanism shown in Figure 4a. (e) The true slab effects, involving strong downdip defocusing toward the northwest, present in Figure 4d. (f) The incorrect slab effects, obtained by using the biased focal mechanism to correct the data in Figure 4d. The slab defocusing is still present but is reduced by trade-off with the source mechanism.

weak and scattered patterns. The events of 5 September 1970 (event 6) and 29 January 1971 (event 7) are located in close proximity and thus may be used to establish the stability of the amplitude patterns. Both do show a northwesterly zone of focusing, with scattered defocusing toward the northeast and south, but clearly, there is significant scatter between events. This may arise from acute sensitivity to position within the slab, from noise contributions to the amplitudes, and from errors in the various corrections. It is worth noting that there was significant scatter in travel time residuals between these two events in the study of *Pankow and Lay* [1999] that could not be explained by simple slab models. Relatively weak patterns are present for the other deep events, which could either be attributed to weak velocity gradients in any deep slab extension or evidence that the slab does not penetrate deeply into the lower mantle. The level of scatter in these patterns is such that we cannot expect to match individual amplitudes with simple thermal slab models, so our modeling approach will be to qualitatively fit the general patterns of focusing and defocusing and to avoid predicting stronger patterns than are observed.

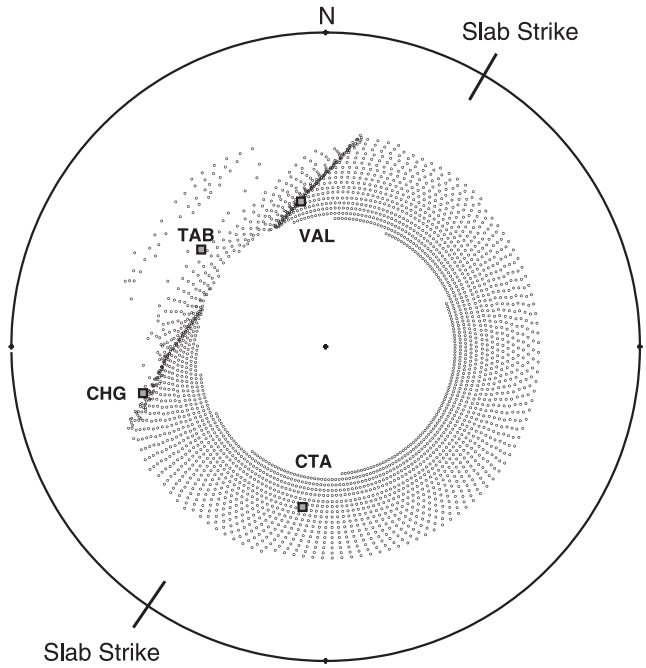

Figure 6. A ray map generated by dynamic ray tracing from the event of 1 December 1967 through a tabular structure ($\mathbf{A}_{PD}$ = 0.0). The geographic coordinates for the endpoint of each ray are projected onto a lower hemisphere projection and plotted similar to an amplitude residual sphere, as a function of takeoff angle and azimuth. The circumference of the circle corresponds to a takeoff angle of 60°. The position of the strike of the slab is given by heavy lines that intersect the circle. For this event a shadow zone is seen in the downdip direction, the northwest quadrant. There are also two areas of intense ray sampling. These are interpreted as caustics. The squares are WWSSN stations plotted near the rays that will be summed to form the amplitude at each station.

3. Modeling

[19] The data in Figure 2 indicate that patterns induced by near-source slab structure are likely to involve complex three-dimensional effects, not simple downdip dependence on takeoff angle. While modeling this complexity offers the promise of providing new constraints on slab structure, fully three-dimensional simulation for many models for appropriate wavelengths presents a great challenge. Numerical methods that include complete wave field interactions with slab structure for the small-scale, strong velocity contrast models of interest are not routinely available yet. Ray theory and eikonol methods that suffice for travel time calculations can be used to explore many models but do not provide reliable finite frequency amplitude calculations, so we must compromise somewhat in our modeling. We seek to model the amplitude residual spheres using programs developed by *Sekiguchi* [1992]. We begin with dynamic ray tracing and then use the ray solutions from that method to calculate Gaussian beams. The limitations of this approach are well established [*Cormier*, 1989], and we are conservative in our modeling ambitions.

3.1. Dynamic Ray Tracing

[20] To begin the modeling process, we shoot rays as a function of takeoff angle and azimuth from each source location in a slab model embedded in a flattened spherical Earth structure using dynamic ray tracing [*Cerveny and Hron*, 1980; *Cerveny*, 1985a, 1985b; *Cerveny and Psencik*, 1979]. As our model space involves three-dimensional heterogeneity only in the immediate source region, the Earth-flattening effect is minor around the slab and is well-behaved in the deep mantle where the rays turn in homogeneous PREM structure. Near-source effects of stretching of velocity gradients in the flattened model are generally small but may lead to some inaccuracy of the *SH* predictions, particularly in the along-strike direction. The range of takeoff angles and the number of rays considered are determined by the distance range of the stations and by the number of rays required to give stable results for intermediate period (5–15 s) *S* wave synthetics using PREM. Attenuation is not included in the synthetics since we have already removed this effect from the data by the correction for differential attenuation predicted by PREM. The velocity models were extracted from intrinsically smooth thermal structures and interpolated with cubic splines to ensure two continuous spatial derivatives. No sharp interfaces at the surface or within the slab were allowed, although the code used can handle curved interfaces.

[21] For all sources in each model, ray maps were generated for a regular grid of rays spanning all azimuths and a range of takeoff angles. The ray maps involve lower hemisphere projections of the actual endpoint of each ray in geographical coordinates as a function of takeoff angle and azimuth from the source (for the corresponding ray paths in a homogeneous PREM model). Using this lower hemisphere projection, it is easy to see areas of focusing and defocusing (Figure 6), and how they relate to the strike of the slab. For the example in Figure 6 a large shadow zone develops toward the northwest, where little energy arrives. This region is bounded on either side by linear caustics originating by refraction from the upper surface of the

Table 2. Example Amplitude Calculations[a]

Stations	APD	Amplitude log(base 10)	Stations	APD	Amplitude log(base 10)
CHG	0.0	−4.04	TAB	0.0	−4.52
	1.0	−40.55		1.0	undefined
	10.0	−5.57		10.0	−6.87
	100.0	−4.07		100.0	−4.56
	1000.0	−4.04		1000.0	−4.52
CTA	0.0	−4.04	VAL	0.0	−3.96
	1.0	undefined		1.0	−5.31
	10.0	−6.30		10.0	−3.60
	100.0	−4.04		100.0	−3.96
	1000.0	−4.04		1000.0	−3.96

[a] Stations are those shown in Figure 6. Undefined amplitudes are those where the sum was 0.0. Therefore log(base10) is undefined.

subducting slab. The geographical coordinates of Earth's surface are mapped into this lower hemisphere, so we can consider specific station amplitude effects. For example, we expect station CTA to have an average amplitude, station VAL to be focused, station TAB to be defocused, and station CHG is uncertain until finite frequency effects are accounted for. We can thus use ray maps qualitatively to check the Gaussian beam computations and to detect areas where those computations may fail due to inadequate ray sampling. In general, we find that there is a good qualitative agreement between simple ray density considerations and Gaussian Beam calculations, although the latter involve significant smoothing and averaging relative to optics predictions as desired.

3.2. Gaussian Beam Method

[22] The main benefit of the Gaussian beam method over dynamic ray tracing is that the existence conditions for Gaussian beams [*Cerveny and Psencik*, 1983] guarantee that Gaussian beams have no singularities. This in turn guarantees more reliable amplitude calculations at caustics and in shadow zones, although poor estimates are provided when ray density is very low. Gaussian beams are calculated by an integral superposition of all rays passing within a specified region around the receiver. Following *Cerveny* [1985a, 1985b],

$$\mathbf{u} = \int\int_D \mathbf{U}^{\mathrm{RAY}} \left|\det \mathbf{Q}^R\right| \left[-\det\left(\mathbf{M}-\mathbf{M}^R\right)\right]^{1/2} \cdot \exp\left[i\omega\left(\tau \pm \mathbf{q}^T\mathbf{M}\mathbf{q} - t\right)\right] d^2\gamma, \quad (1)$$

where the quantities $\mathbf{U}^{\mathrm{RAY}}$, $\mathbf{M}^R$, and $\mathbf{Q}^R$ correspond to the ray solution calculated by dynamic ray tracing, $\mathbf{M}$ is a complex-valued matrix of the Gaussian beams, D represents the area around the location where the seismogram is calculated, and γ is a ray parameter. The amplitudes of the rays are weighted such that the amplitude profile in the plane perpendicular to the central ray has a Gaussian distribution.

[23] Even though the existence conditions might be met, to get accurate seismograms, special attention must be paid to the beam parameter [*Weber*, 1988]. This parameter specifies the width and the phase front of each Gaussian beam. In equation (1) this parameter is part of the matrix $\mathbf{M}$. *Cerveny* [1985a, 1985b] discusses how to choose $\mathbf{M}$. We follow the case for a heterogeneous medium with curved interfaces: Re $\mathbf{M}(0) \neq 0$ and Im $\mathbf{M}(0) \geq 0$, where

$$\mathrm{Re}\ \mathbf{M} = -\mathbf{G}^{-1}\left[v^{-1}\cos\theta\mathbf{D} + \mathbf{E}\right]\left(\mathbf{G}^T\right)^{-1} \quad (2)$$

$$\mathrm{Im}\ \mathbf{M} = C\left\{\left[\mathbf{M}^R - \mathrm{Re}\ \mathbf{M}\right]^2 + \mathbf{A}^2{}_{\mathrm{PD}}\right\}^{1/2}, \quad (3)$$

where θ is the incident angle of the ray at the interface, $\mathbf{G}$ is a 2×2 transformation matrix between the ray-centered and local Cartesian coordinate systems, $\mathbf{D}$ is a curvature matrix for the interface, $\mathbf{E}$ is a matrix specifying the velocity gradients, C is a positive constant, and $\mathbf{A}_{\mathrm{PD}}$ is some optional real-valued, symmetric positive-definite matrix which specifies the lower bound of Im $\mathbf{M}$. For a heterogeneous medium, $C = 1$ and $\mathbf{A}_{\mathrm{PD}} = 0$ give the most stable results [*Cerveny*, 1985a, 1985b; *Sekiguchi*, 1992].

[24] To test the effect of beam widths in our modeling, we varied the value of $\mathbf{A}_{\mathrm{PD}}$. This varies the lower bound of Im $\mathbf{M}$ (Table 2). As $\mathbf{A}_{\mathrm{PD}}$ gets larger, the calculated amplitude converges to the amplitude that is obtained when $\mathbf{A}_{\mathrm{PD}} = 0.0$. Figure 7 shows the rays and contributions of each ray for each of the stations identified in Figure 6, using beam parameters that provide stable results for a homogeneous model. This involves inclusion of beam contributions down by 2–3 orders of magnitude relative to the largest contributor. This includes rays sampling relatively large angular distances around each receiver, as indicated. In each case, there appear to be enough rays to generate a stable 10-s pulse amplitude, and changes in the beam widths do not cause rapid fluctuations in the calculated value for each station. The displacement pulses produced by the beam sums are shown at the bottom, and while large relative amplitude variations are found, corresponding well with ray density, the wave shapes appear stable and the beam sums appear to have converged.

[25] Once the amplitudes for all stations for a particular event are calculated for a given slab model, a baseline is removed. Instead of removing the mean calculated using all stations, the baseline value found in a stable part of the residual sphere is calculated and this mean is removed from all stations. The stable part of the residual sphere is determined by examining the ray maps. This procedure is used because in areas of shadow zones and caustics the individual amplitudes can become very large, positive or negative, such that a few observations can dominate the average. Thus, for the Gaussian beam synthetics the amplitude residual spheres represent the difference from a base model, PREM, just as

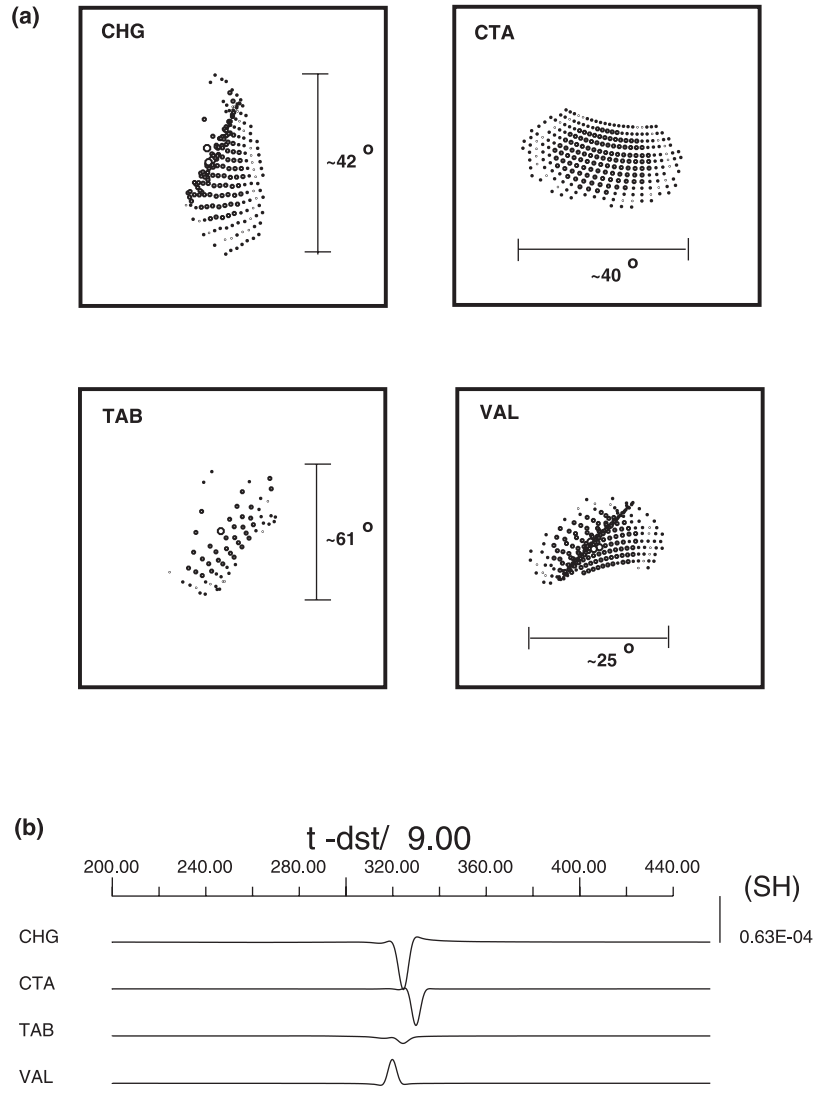

Figure 7. (a) Enlarged sampling areas for the stations CHG, CTA, TAB, and VAL given in Figure 6. The size of each endpoint indicates the contribution of that ray to the amplitude calculated using Gaussian beams. The larger the circle, the larger the contribution. The amplitudes of the most distant contributors are down by 2–3 orders of magnitude or more relative to the closest rays. The angular distances indicated in each plot indicate the separation of endpoints in the set of rays contributing to the synthetic in each case. (b) Synthetic displacement pulses produced by the Gaussian beam summation for each station, plotted at reduced travel times. Note the stable shape of the pulses, suggesting convergence of the sum, and the large amplitude variations of the wavelets, consistent with the ray distribution.

we sought to achieve in the data processing. If we use the same stable region to demean the data, small shifts relative to the overall data mean occur, but this is dependent on averaging of highly scattered values, so we prefer to shift the data by the overall mean. The data simply do not show such pronounced, one-sided patterns as the synthetics.

4. Results

[26] In the modeling process we explored many different slab structure parameters. We began with previously determined Kurile slab models from arrival time studies, recognizing that there is uncertainty in where to embed the sources within these models. Geometric parameters such as slab dip, penetration depth, and across-slab thickness were varied, and we introduced tears and flattening of the slab model as needed, although the spline interpolation of velocities keeps gradients fairly smooth. The peak absolute velocity anomaly was varied, as well as the across slab velocity profile, which was parameterized by an asymmetric error function. We did not introduce internal slab layering or structures such as mantle discontinuities or wedges of low-velocity material that could represent metastable phase transitions. For this paper, our goal was to appraise whether simple thermal slab structures could match the amplitude observations, recognizing that enhanced velocity gradients at compositional and phase boundaries and complex internal structure of the slab may well exist. The strong velocity contrasts at the 410-km and 660-km discontinuities (expected to be displaced upward and downward within the cold slab, respectively) serve to

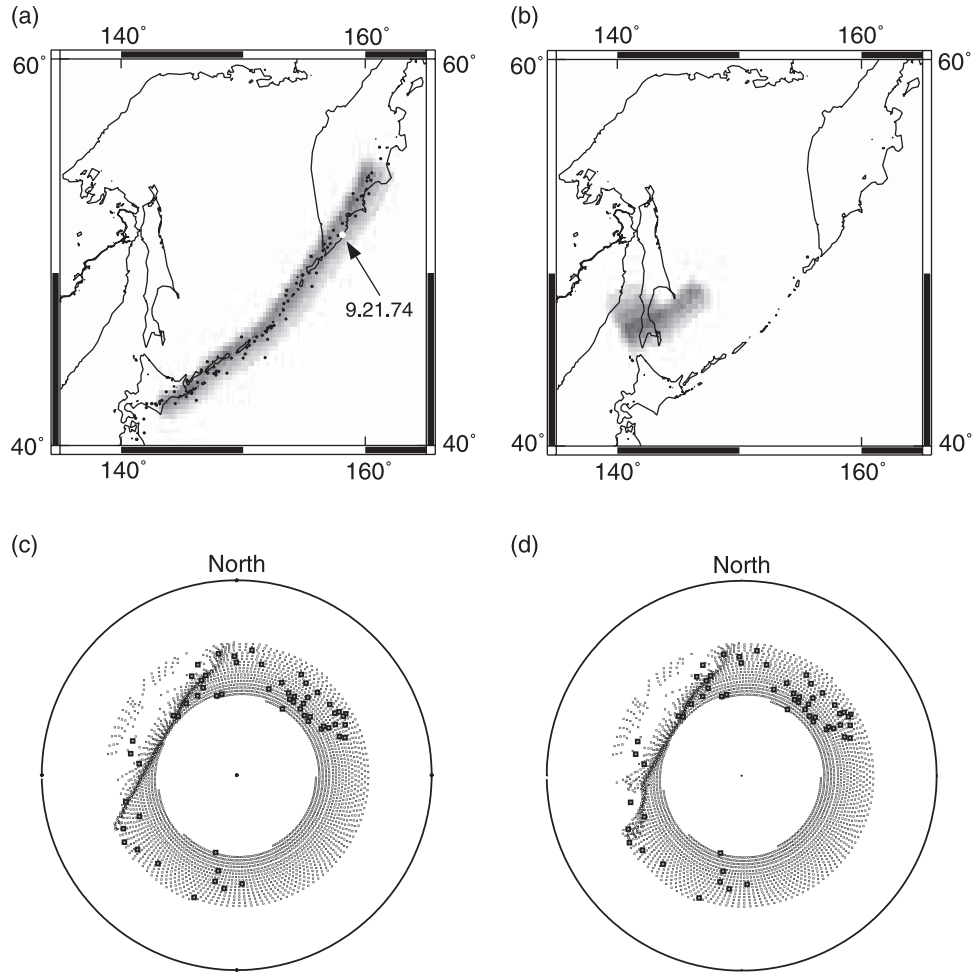

Figure 8. Mercator projections of the study area with a slab model overlain and ray maps for two different models. (a) Depth section of the model at 100 km. (b) Depth section of the model at 700 km. (c) *S* wave ray endpoints for the event of 21 September 1974 shot through a variation of the model that stops at 670 km along the entire strike. (d) *S* wave ray endpoints for the event of 21 September 1974 shot through the model shown in Figures 8a and 8b. The deep extension seen in Figure 8b extends to 1000 km.

enhance and diminish velocity contrasts between the slab and surrounding mantle, respectively. To first order, this is accommodated in adjusting the strength of slab velocity, but any effects of dipping phase boundaries are not accounted for. As discussed below, more realistic slab modeling is probably required for full exploitation of amplitude observations, but given the present uncertainties in equilibrium and metastability of slab phases [e.g., *Bina et al.*, 2001; *Collier et al.*, 2001], a full exploration of thermochemical slab models is beyond the scope of this paper. Similarly, we did not explore anisotropic models of the slab [e.g., *Kendall and Thomson*, 1993], although it is possible that this contributes to *S* waveform complexity [e.g., *Vinnik and Kind*, 1993]. Forward modeling was used, as the problem proves highly nonlinear, particularly with respect to event location within the slab structure. We first tried to constrain the overall slab geometry and velocity anomaly for source locations in the upper side of the slab, then optimized the source location relative to the velocity gradient. The three-dimensional, laterally finite geometry of the arcuate dipping slab produces complex patterns that complicate finding a preferred model, but it is this very complexity that provides the potential for seismic wave amplitudes to help constrain slab structure.

4.1. Three-Dimensional Ray Effects

[27] Figure 8 shows ray maps from the event of 21 September 1974 (event 13, depth of 121 km) for two nearly identical models. The only difference between the two models is the presence of a deep extension in the southern part of the subduction zone (Figure 8b). Figure 8c is the ray map generated for a slab model that terminates at 670 km depth along the entire slab. Figure 8d is the ray map for the model with the deep extension in the south. Comparing the WSW region of both ray maps, one notices a localized zone of defocusing in Figure 8d. This example demonstrates that even distant events may constrain deep slab geometry due to long paths along strike that can intersect deep extensions of the slab. In this case, the rays that sense the deep slab extension traverse the back of the slab, exiting the structure and then being deflected by the high velocity extension into the lower mantle. This presents the complication that the entire slab geometry can influence the amplitude pattern,

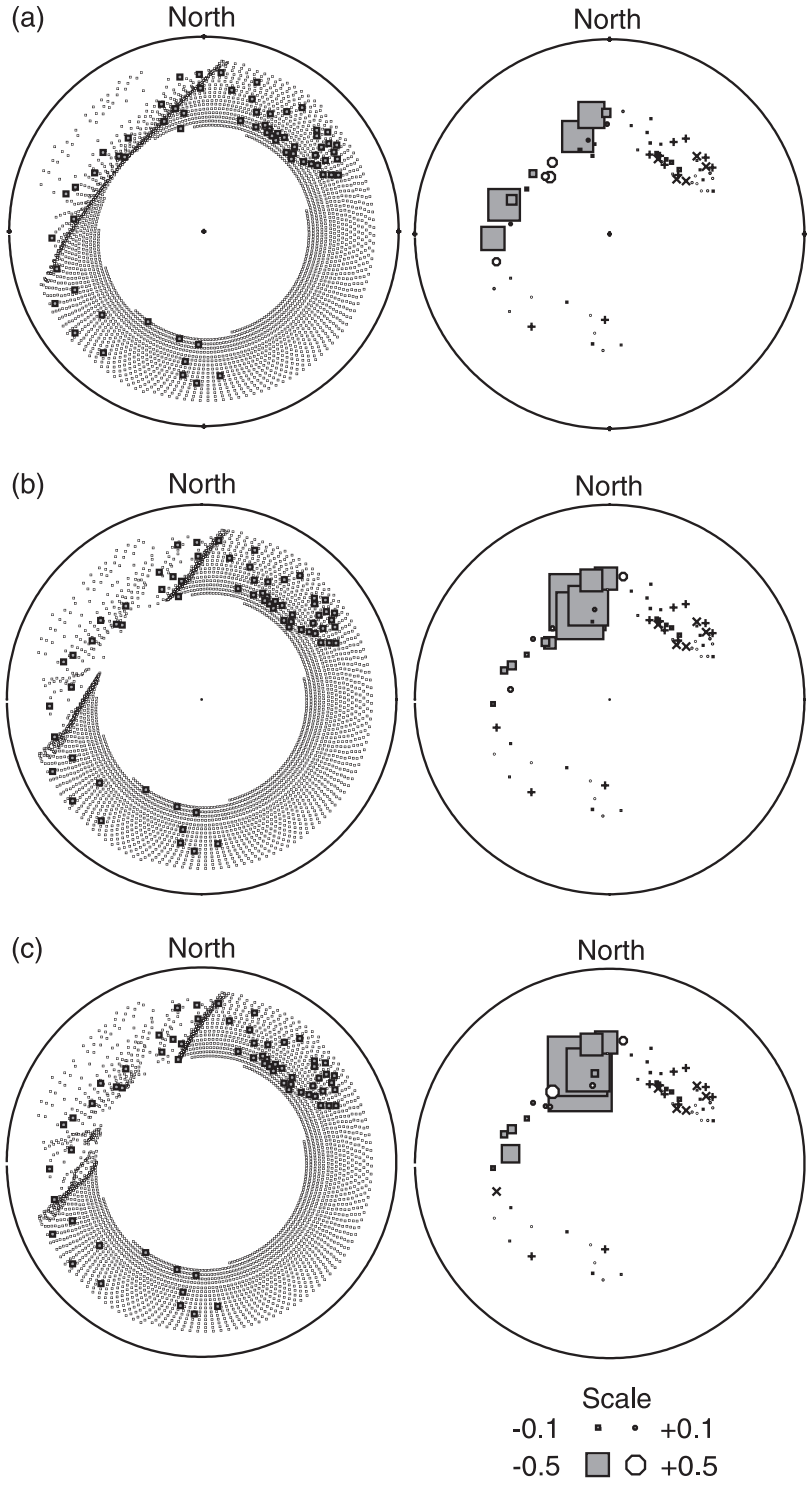

Figure 9. *S* wave ray maps and amplitude residual spheres generated by varying the penetration depth of a tabular model. The event origin was near 1 December 1967. (a) penetration depth of 670 km, (b) penetration depth of 1000 km, and (c) penetration depth of 1200 km. The squares in the amplitude residual spheres are smaller than average amplitudes, the circles larger than average amplitudes, and the crosses (positive) and pluses (negative) residuals that are less than ±0.1. The squares in the ray maps are station locations.

and care must be taken to avoid attributing all fluctuations to very near-source geometry.

[28] Two parameters with particular importance for the modeling of amplitudes are slab penetration depth and event position relative to the across-slab velocity gradient. To explore the effects of penetration depth, we fixed the geometry of the slab and then varied the depth extent. We first consider a tabular slab structure with a peak velocity

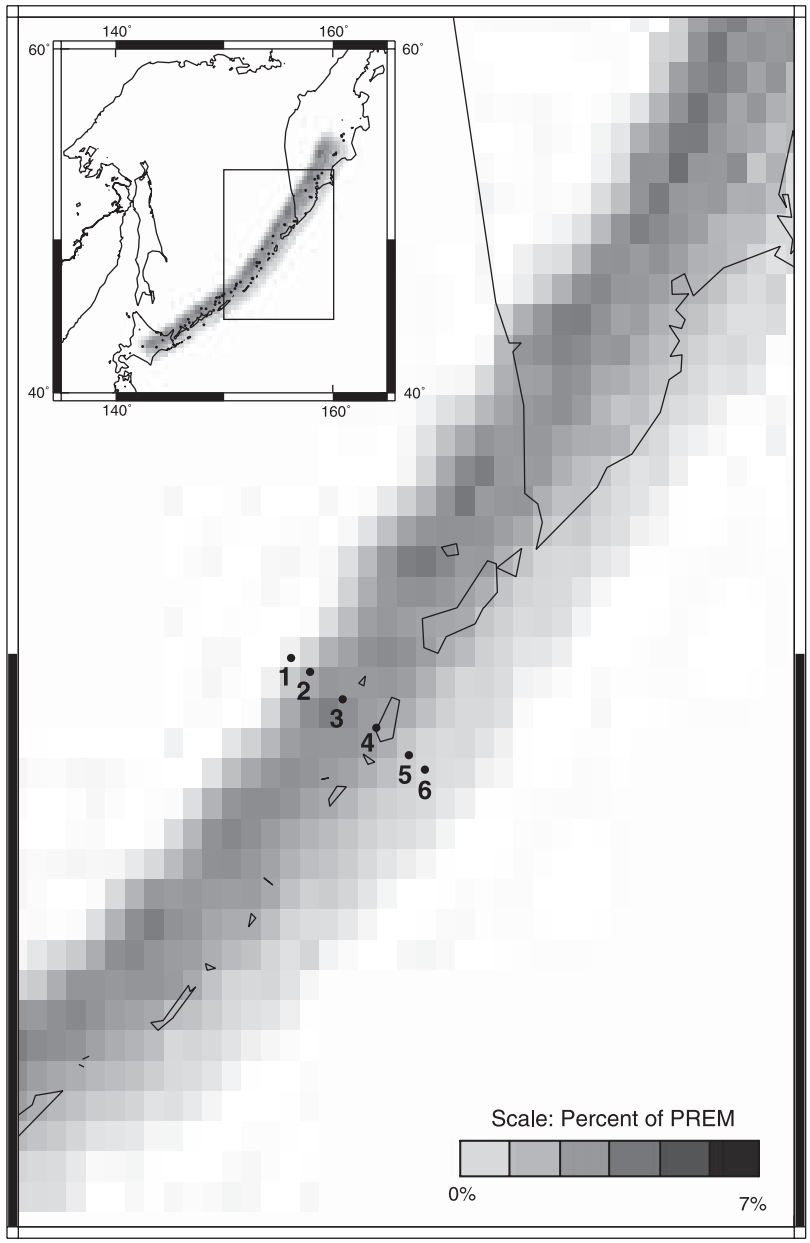

Figure 10. Enlarged Mercator projection of the study area overlain with a depth cross section at 150 km. The inset shows the location of the blowup relative to the entire zone. The solid circles are event positions for testing the effect of lateral position relative to the slab velocity gradient.

anomaly of 4% higher than PREM ambient mantle above 670 km and 2% higher below 670 km, similar to the travel time model of *Pankow and Lay* [1999]. Figure 9 shows the effects of allowing the maximum penetration depth for the steeply dipping leading edge of the slab to increase from 670 to 1200 km on ray positions and Gaussian beam amplitude calculations for *S* waves from a source at 143 km depth. There is no sensitivity to deeper slab extensions for the *S* paths, but some *ScS* paths may still be affected. For the slab that extends to 670 km depth (Figure 9a), there is strong downdip defocusing toward the northwest, which produces the band of very low amplitudes that parallels the caustic along which there is some focusing. In general, the Gaussian beam calculations do not show dramatic focusing effects near caustics, and when there are strong shadow zones, the defocusing effects tend to be somewhat unstable and are likely overestimated. Nonetheless, we think the relative behavior between models can be relied on as a qualitative guide. As the penetration depth increases, the defocused area broadens directly downdip, and the caustics rotate a bit. This concentrates the defocused amplitudes in the downdip direction, and even less focusing by caustics is observed. For the events above 200 km depth the data (Figure 2) show more uniform bands of defocusing for stations toward the west, which tends to be more consistent with strong slab anomalies extending to only 670 km depth.

[29] To test the effects of event position relative to the velocity gradient, we placed the source for 1 December 1967 (event 3, depth of 143 km) at various positions across a slab model (Figure 10). The resulting ray maps and amplitude

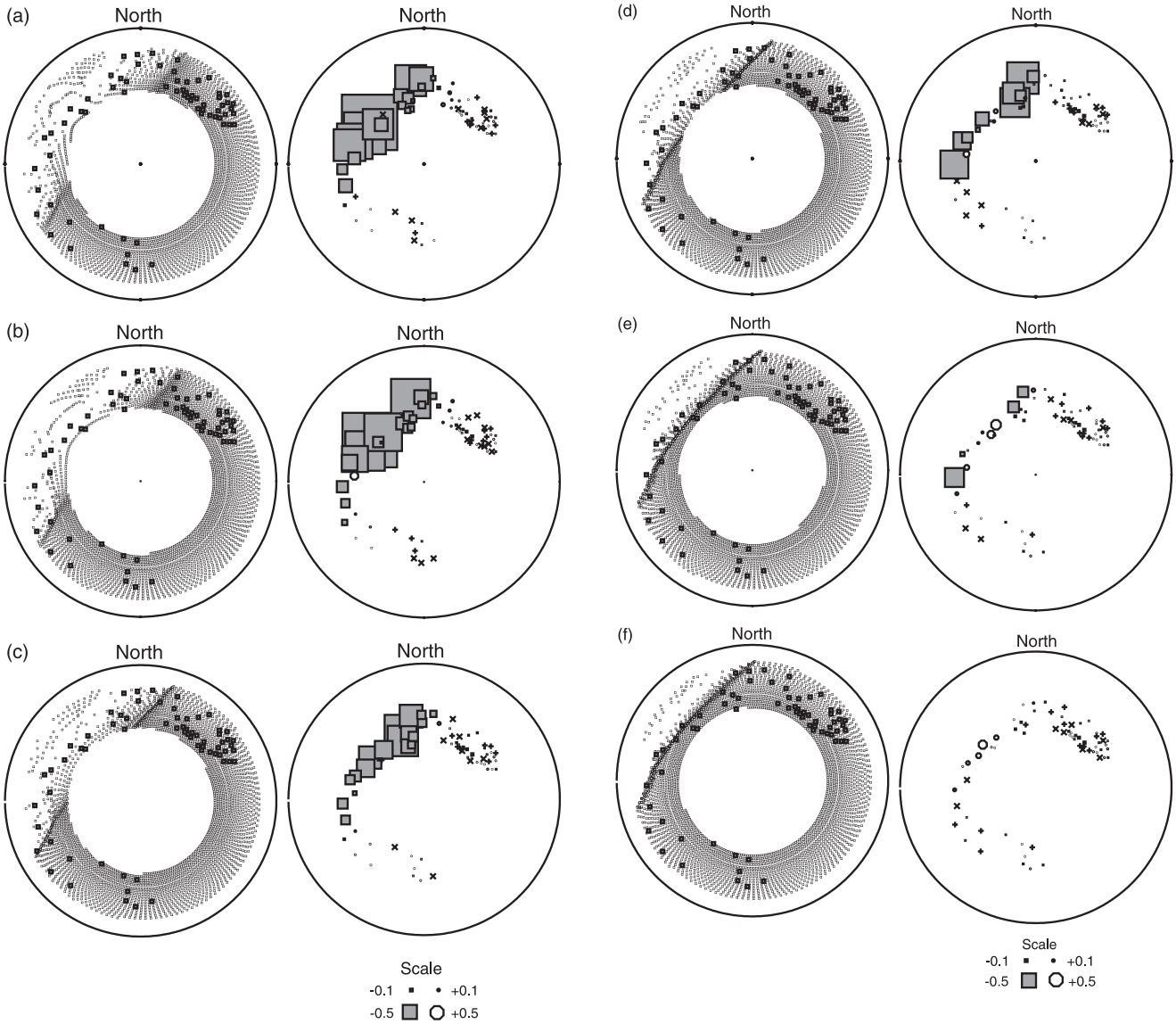

Figure 11. S wave ray maps and amplitude residual spheres generated by varying the lateral position of 1 December 1967 in a tabular model. Event locations are shown in Figure 8. (a) Location 1, (b) location 2, (c) location 3, (d) location 4, (e) location 5, and (f) location 6. The squares in the amplitude residual spheres are smaller than average amplitudes, the circles are larger than average amplitudes, and the crosses (positive) and pluses (negative) are residuals that are less than ±0.1. The squares in the ray maps are station locations.

residual spheres are shown in Figure 11. As the event moves from the top of the slab to the base of the slab, the position of the caustic migrates toward the northwest, gradually moving the defocused zone out of the range of the *S* wave paths. The amplitude pattern is clearly very dependent on the source location relative to the velocity model. Note that in order to produce focusing toward the northwest (as seen in the intermediate depth event data in Figure 2), rather than strong defocusing, the source must be in the central or bottom portion of the slab. This allows us to rule out source locations near the top of the slab for the intermediate depth events.

4.2. Final Model

[30] We systematically considered a wide range of slab parameters, finding that it is difficult to match many of the amplitude features with slabs that extend into the lower mantle with strong velocity heterogeneity. In fact, many of the amplitude features cannot be matched at all by the class of slab models considered, particularly the variations observed out the backside of the slab. There is an uncertainty in the absolute baseline for the observations, such that the magnitude of focusing or defocusing is not resolved, but there are certainly variations in the data at azimuths for which simple slab models predict no variability. This raises the question of how well source radiation pattern and distant propagation effects have actually been suppressed? Also, there is rapid small-scale scatter in the data that can only be qualitatively matched, even if we allow for kinks and tears in the slab. Introduction of internal slab structure may improve the modeling of such features, but that is left to

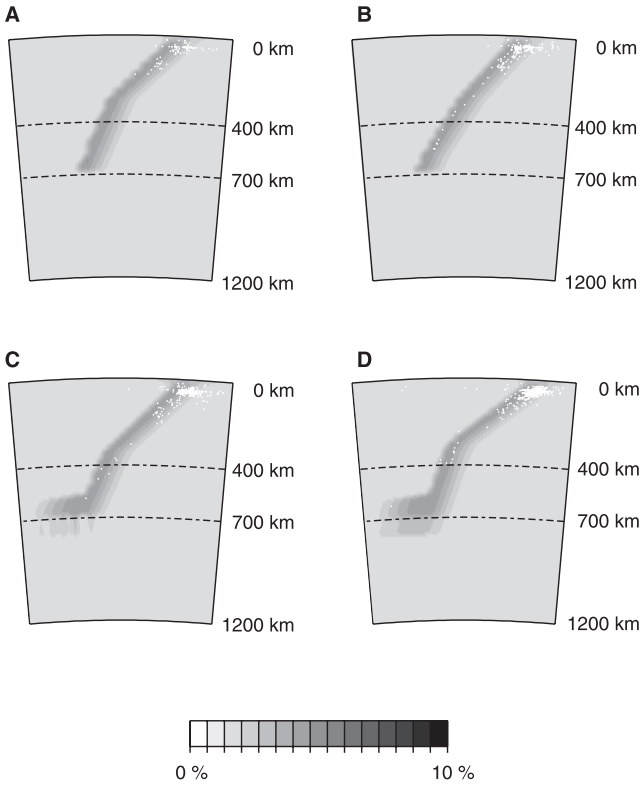

Figure 12. Cross sections of the preferred model generated in this study. The profiles correspond to the dashed lines in Figure 1. Seismicity locations from the monthly listings of the U.S. Geological Survey are superimposed on the velocity model.

future studies. Nonetheless, certain aspects of the data are successfully modeled, and in particular, the data are not consistent with certain classes of structures.

[31] The final model determined in this study (Figure 12) is defined by a thermal anomaly with an asymmetric error function that peaks at 4% larger than PREM ambient mantle 25 km from the top of the slab. The total width of the anomaly averages 140 km. The slab dip ranges from 40° to 50° above 300 km and increases in dip to 60°–80° below 300 km. The slab is a tabular feature that stops at 670 km in the northern half of the subduction zone, and in the southern half the slab is deflected along the 670-km discontinuity, with the southernmost portion of the slab extending down to ~750 km depth. While there may be more extensive slab material in the lower mantle under this region, as suggested by some arrival time studies, our modeling suggests that it does not involve simple tabular structures with several percent velocity anomalies, or else it would produce amplitude patterns that are not observed.

[32] The amplitude residuals computed for this model and for two previously determined arrival time models, DG (a shear wave adaptation of the *P* wave model of *Ding and Grand* [1994]) and PL (tabular model from *Pankow and Lay* [1999]), are compared with the data in Figure 13. For the models DG and PL the source locations were constrained to those used in the travel time analyses. Effectively, these define the starting point for our modeling, which included perturbing the slab structure and the event locations. For the events shallower than 200 km deep (Figures 13a–13d), PL overpredicts the defocusing (note the variations in the scale), and the Gaussian beam calculations are not reliable. This suggests that the basic slab velocity anomaly is too large; for PL it peaks at 5% faster than PREM. Also, for the shallowest events, PL and DG predict extensive defocusing in the downdip direction where the observations often show some focusing. Focusing, or at least reduced defocusing, in the downdip direction for these events was obtained in this study by locating these shallower events in the lower half of the slab. This improves the match to the general azimuthal pattern, with relatively larger amplitudes toward the northwest and defocusing concentrated toward the west for most events, as observed (except for the event of 19 July 1986 (event 28) in Figure 13d). Some of the gradients between *ScS* and *S* phases at a given azimuth are matched, but overall, the *ScS* behavior tends to be underpredicted.

[33] The events near 400 km depth are fairly well matched by the preferred model (Figures 13e and 13f). Strong focusing toward the northwest for the event of 21 June 1978 (event 16, Figure 13e) is produced in the preferred model by locating the event at the upper boundary of the slab. The *ScS* amplitudes are not fit as well as the *S* amplitudes though. Neither of the arrival time models predict focusing for this event for the default locations. The amplitudes for the event of 10 July 1976 (event 14, Figure 13f) are moderately scattered, with a steeply dipping band of low amplitudes. The synthetics for the preferred model generally match this band and predict some focusing to the west, whereas the travel time models do not match the data well.

[34] The four deepest events (Figures 13g–13j) show weak observed patterns, with three of the four events showing weak focusing toward the northwest. This is matched fairly well by the preferred model for the event of 5 September 1970 (event 6, Figure 13g) but underpredicted in strength for the events of 1 January 1971 (event 7, Figure 13h) and 1 February 1984 (event 24, Figure 13j). The tabular slab in model PL extends to a depth of 800 km in the north and to 700 km in the south, whereas the slab in the preferred model stops as 670 km depth in the north and deflects horizontally in the south. The PL model thus predicts more concentrated downdip defocusing than the preferred model, but this is not observed in the data. The absolute velocity anomalies in the PL model in the lower mantle are only as large as 2%, and this already overpredicts defocusing effects. Strong slab anomalies, such as in the early residual sphere models of *Creager and Jordan*, [1984, 1986], predict far greater defocusing, which is not observed. The DG model differs from the two other models in that in the northern half of the region at depths greater than 670 km the slab broadens by up to a factor of 3 of more. With only a 2% shear velocity anomaly in the deep extension of the slab, the velocity gradients are too weak to produce much amplitude effect. Thus model DG fails to match the weak pattern of focusing that is observed, but it also demonstrates that the slab need not terminate at 670 km depth; if it broadens as it penetrates, it will not produce strong defocusing.

[35] The comparisons with the arrival time based models in Figure 13 were not optimized by perturbing the source

Figure 13. A comparison of amplitude residual spheres for this study and two previous studies. (left) Data, (left middle) results from this study, (right middle) amplitude residuals calculated for the model of *Ding and Grand* [1994], and (right) the results using the tabular model from *Pankow and Lay* [1999]. Note the smaller scale used in Figures 13(right middle) and 13(right). The squares are smaller than average amplitudes, the circles larger than average amplitudes, and the crosses (positive) and pluses (negative) residuals that are less than ±0.1. For (a) 24 July 1983, (b) 21 September 1974, (c) 1 December 1967, (d) 19 July 1986, (e) 21 June 1978, (f) 10 July 1976, (g) 5 September 1970, (h) 1 January 1971, (i) 20 April 1984, and (j) 1 February 1984.

location in the slab, as was done in our modeling, and it is reasonable to seek a best fit by moving the location without changing the structure. This is essentially the essence of our modeling, as we began with the travel time models and default event locations in the slab. Figure 14 illustrates the effect of moving the source location in the tabular slab model of *Pankow and Lay* [1999] for the intermediate depth event of 1 December 1967 (event 3). Strong downdip defocusing is predicted for all locations in the slab with the exception of in the lower portion of the slab where rays can exit the slab quickly. This closely parallels the results in Figure 11 for a simplified tabular model. If the slab anomalies are held fixed, and as strong as in the travel time models, such relocations of the source are needed in order to avoid predicting stronger amplitude patterns than observed, and indeed, this occurs for several of our best fitting solutions. Our basic point in making the comparisons with default locations in Figure 13 is to demonstrate the prob-

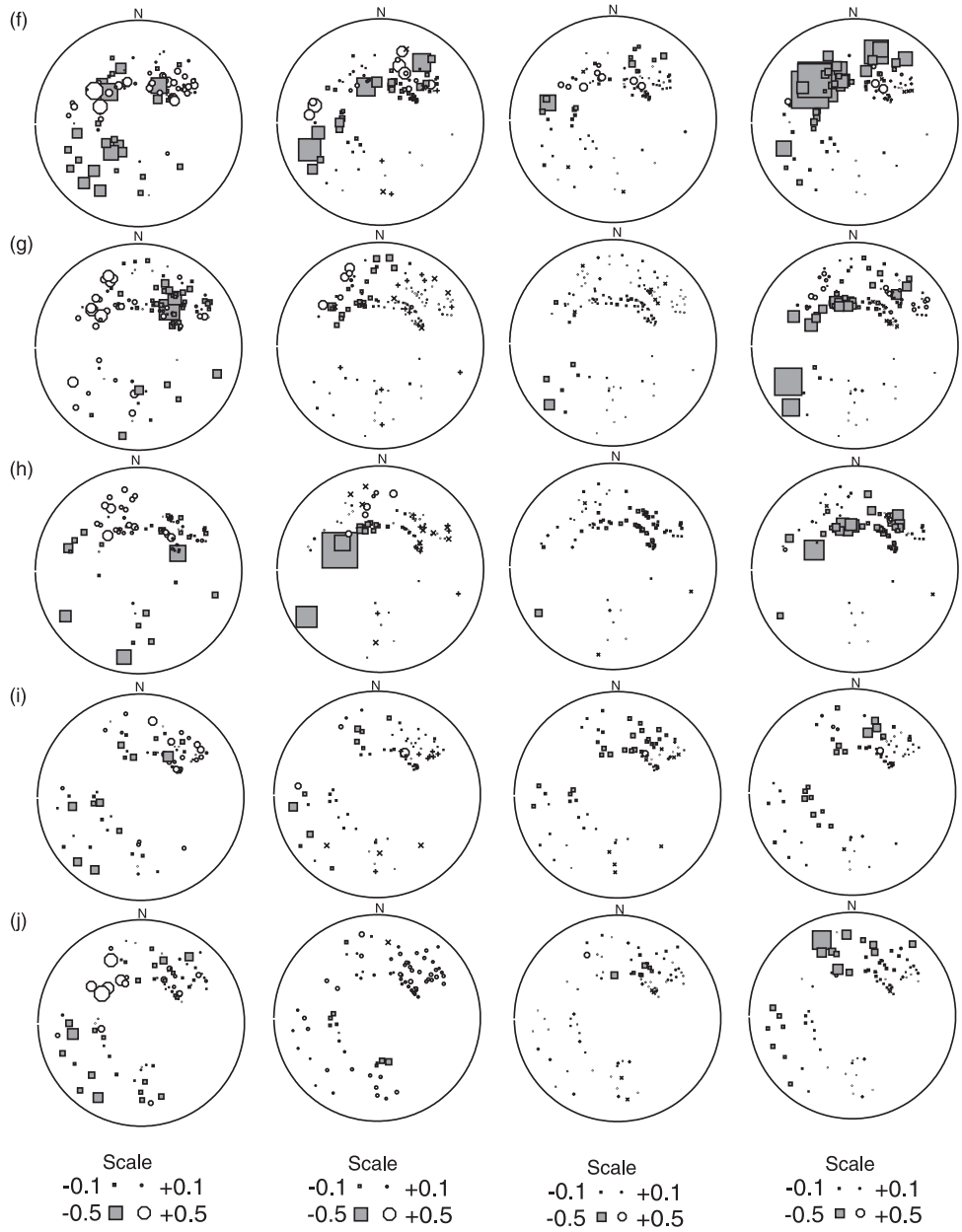

Figure 13. (continued)

lems encountered when using travel time derived models to predict the amplitudes. Relocation may improve the fit to the amplitudes, but one is no longer assured that the arrival time data are well fit.

4.3. Arrival Times

[36] The *S* wave amplitude modeling for the Kurile slab yields a preferred model with a very simple upper mantle slab structure compared to arrival time results. It is useful to take the resulting model and to predict arrival time variations for it to establish how consistent the model is with arrival time observations. The travel times for our slab model were generated using a three-dimensional finite difference code [*Vidale*, 1990] and were processed in the same manner as in *Pankow and Lay* [1999]. The arrival time anomalies are compared with observations and the results of the PL tabular slab model in Figure 15. Noting the different scales in Figure 15, it is apparent that the amplitude-based model underpredicts the arrival time variations for all events, even though the basic pattern is matched for most events. The arrival time based model provides a better overall fit to the data, although there are significant discrepancies. Simply increasing the average slab velocity structure of the amplitude-based model to scale up the arrival time anomalies leads to overprediction of defocusing effects. This suggests a strategy of simultaneous modeling of amplitudes and arrival times, exploiting the differences in sensitivity to velocity gradients provided by the two data types. The main problem for this approach is that the data processing of amplitudes and arrival times involves corrections with substantial uncertainty and some of the discrepancies between amplitude and arrival time residuals may be

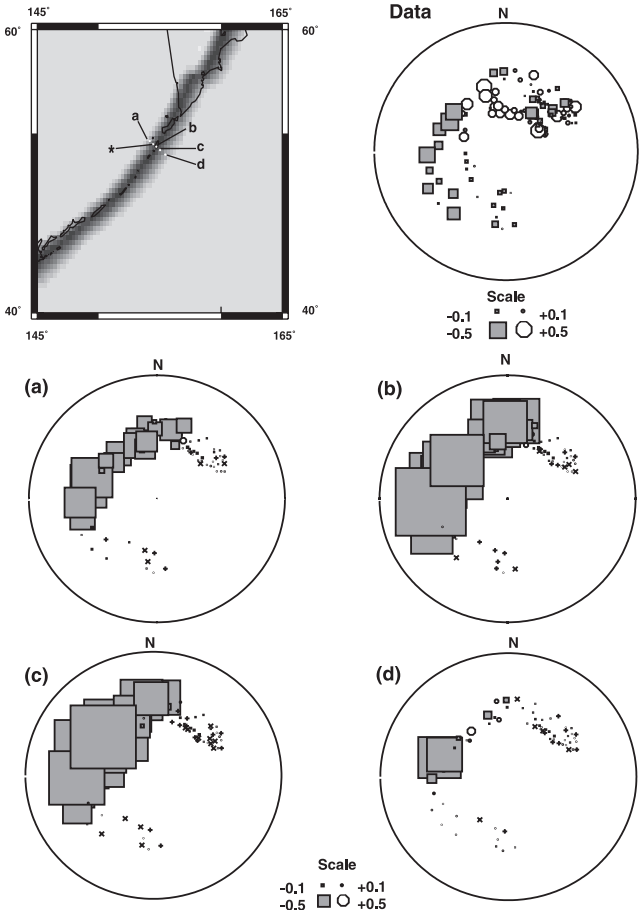

Figure 14. Effects of moving the source location relative to the velocity structure of the tabular slab model of *Pankow and Lay* [1999] for the 1 December 1967 event. The map indicates the fast slab anomaly and the position of the source associated with the amplitude residual spheres shown below. The star indicates the source location used in Figure 13c (right). The data pattern is reproduced in the upper right corner. The simple slab structure predicts strong defocusing effects for all locations except position (Figure 13d), at the lower edge of the slab, where most ray paths quickly exit the slab. This results in a pattern more similar to the model from this paper (Figure 13c, left middle), obtained with a weaker slab heterogeneity.

the result of inadequate corrections (note that the arrival time predictions for the amplitude-based slab model for the event of 21 June 1978 (event 16) in Figure 15e are very different than the data or the PL model, even though the amplitudes are well matched (Figure 13e). Simultaneous modeling of amplitudes and travel times will likely also require more complex slab model parameterizations, and this will be considered in future efforts.

5. Discussion and Conclusions

[37] The first set of complete teleseismic *SH* wave amplitude residual spheres has been produced for ten events in the Kurile slab. Corrections have been applied for geometric spreading, differential attenuation in the PREM model, source radiation pattern, and receiver/upper mantle effects in an attempt to isolate the near-source slab contributions. While there is substantial scatter in the corrected amplitude residual spheres, coherent features with consistency from event to event indicate that near-source effects have been extracted well enough to justify modeling. Three-dimensional dynamic ray tracing and a three-dimensional Gaussian beam method were used to predict amplitude variations for slab shear velocity models. The focusing and defocusing of the *S* phase for eight of the events are well matched in magnitude and relative pattern. For the event of 19 July 1986 (event 28) the focusing in the northwest quadrant could not be fit with any model. We suggest two possible explanations. One, given the distribution of stations for the focal mechanism inversion it is possible that the radiation pattern correction might be incorrect. Two, the geometry of the slab bends near the location of this event. This might induce a pattern too complicated to be mimicked with the thermal model. The event of 1 February 1984 (event 24) is also not well matched. In our model this event is located in the deflected region in the southern half of the subduction zone. It is quite possible that the velocity gradients are not well represented in this area.

[38] In practice, computing Gaussian beam synthetics for the *S* phases is quicker than for *ScS* phases, so much of our modeling focused on the *S* arrivals. It was hoped that in fitting the *S* phase the resulting model would also fit the *ScS* phase as well as the arrival time residuals for both phases. Unfortunately, this is generally not the case. The *ScS* amplitude variations are underpredicted for most events. In order to fit the *S* wave patterns for the shallower events the sources needed to be located near the back of the slab. Since *ScS* has steeper takeoff angles, this phase then rapidly exits the slab material and does not accumulate an amplitude anomaly. For events at depths near 400 km, *ScS* amplitude variation is predicted, but the match to the data is not very good. The events near 400 km depth were located near the top of the slab in order to fit the pattern seen in the *S* data. For these locations the *ScS* phase encounters the slab gradient at different angles than the *S* phase, which causes stronger defocusing than observed. It is also problematic that both *S* and *ScS* amplitude residuals at azimuths opposite in direction to the slab dip are not well modeled. Adding internal structure such as that associated with phase boundaries to the slab can produce scatter in the direction opposite to slab dip [*Pankow et al.*, 2002]. Internal structure more complicated than the thermal structure might also be necessary to fit *S* and *ScS* simultaneously.

[39] The amplitude modeling has established three points regarding slab structure. First, for the along-strike azimuths, slab structure hundreds of kilometers away can produce amplitude effects; thus full slab modeling efforts are required. Also, the observed and predicted patterns are complex, with the entire pattern providing information about the slab geometry. Thus restricting the problem to two dimensions is not adequate. Second, the amplitudes vary systematically based on the penetration depth and velocity gradients within any lower mantle extension of the slab. The weak amplitude pattern, as well as the weak arrival time patterns for very deep focus events, implies that coherent tabular extensions of slab material with a few percent velocity anomaly are probably not present below the

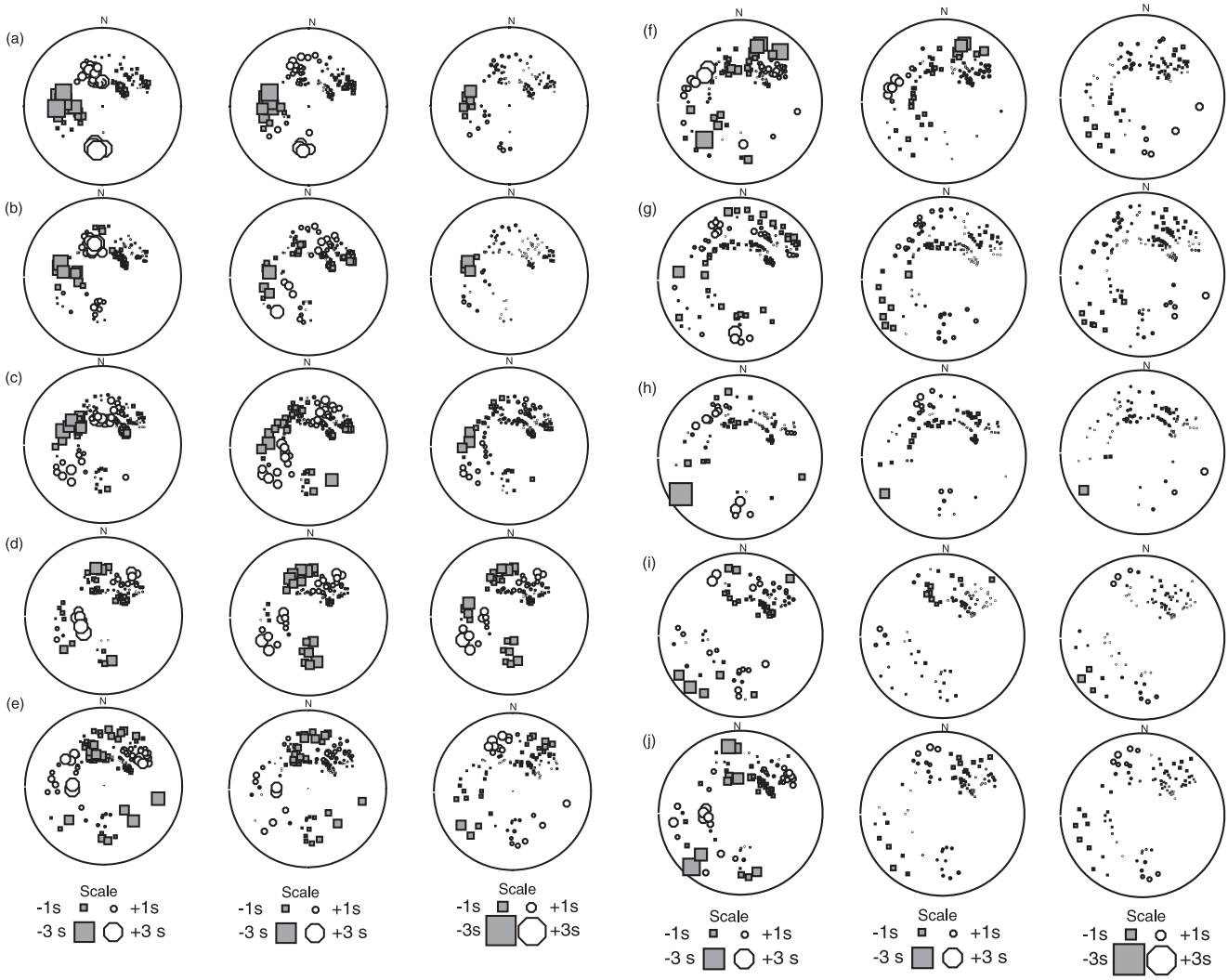

Figure 15. A comparison of arrival time residual spheres for this study and the tabular model given by *Pankow and Lay* [1999]. Squares represent earlier than average times, and circles represent later than average times. (left) Data, (middle) arrival time anomalies calculated for the tabular model from *Pankow and Lay* [1999], and (right) results from this study. Note the larger scale used in Figure 15(right). For (a) 24 July 1983, (b) 21 September 1974, (c) 1 December 1967, (d) 19 July 1986, (e) 21 June 1978, (f) 10 July 1976, (g) 5 September 1970, (h) 1 January 1971, (i) 20 April 1984, and (j) 1 February 1984.

Kurile arc. If significant slab penetration takes place, the slab material is probably broadened, with the lateral velocity gradients being reduced so that the amplitude effects are diminished. This may allow images of lower mantle heterogeneity with lateral dimensions of 300–500 km to be reconciled with slab structures. Third, the location of the sources relative to the internal slab velocity gradient is very important, and the best match for our data was found by placing events above 200 km depth rather deep into the slab and events near 400 km depth near the upper surface of the slab. Different parameterizations of internal slab velocity gradients may modify these inferences.

[40] This was a first attempt at systematic three-dimensional modeling of amplitudes to constrain a slab structure. The next step will be to simultaneously match the amplitudes and arrival times. It appears that allowing for more complex parameterizations of the slab structure will be necessary for this to succeed. This effort will require collecting a large data set of broadband teleseismic amplitude and arrival time data. Special care will have to be taken in the data processing to isolate near-source contributions and to ensure that the amplitude and arrival time information are both constraining near-source structure.

[41] **Acknowledgments.** We thank Shoji Sekiguchi for providing his dynamic ray tracing and Gaussian beam codes and for extensive documentation and testing of these codes on our computers. We also thank Justin Revenaugh and Ru-Shan Wu for time on their computers. Jim Gaherty kindly provided his amplitude observations and many plotting codes. The JGR Associate Editor, Justin Revenaugh, and an anonymous reviewer provided helpful comments on the manuscript. This research was supported by NSF grant EAR-9418643. Contribution 454 of the Center for the Study of Imaging and Dynamics of the Earth.

References

Ansell, J. H., and D. Gubbins, Anomalous high-frequency wave propagation from the Tonga-Kermadec seismic zone to New Zealand, *Geophys. J. R. Astron. Soc.*, *85*, 93–106, 1986.

Beck, S. L., and T. Lay, Test of the lower mantle slab penetration hypothesis using broadband *S* waves, *Geophys. Res. Lett.*, *13*, 1007–1010, 1986.

Bina, C. R., S. Stein, F. C. Marton, and E. M. Van Ark, Implications of slab mineralogy for subduction dynamics, *Phys. Earth Planet. Inter.*, *127*, 51–66, 2001.

Cerveny, V., Gaussian beam synthetic seismograms, *J. Geophys.*, *58*, 44–72, 1985a.

Cerveny, V., The application of ray tracing to the numerical modeling of seismic wavefields in complex structures, in *Handbook of Geophysical Exploration Section I, Seismic Exploration*, vol. 15, edited by S. Treitel and K. Helbig, pp. 1–124, Geophys. Press, London, 1985b.

Cerveny, V., and F. Hron, The ray series method and dynamic ray tracing system for three-dimensional inhomogeneous media, *Bull. Seismol. Soc. Am.*, *70*, 47–77, 1980.

Cerveny, V., and I. Psencik, Ray amplitudes of seismic body waves in laterally inhomogeneous media, *Geophys. J. R. Astron. Soc.*, *57*, 91–106, 1979.

Cerveny, V., and I. Psencik, Gaussian beams and paraxial ray approximation in three-dimensional elastic inhomogeneous media, *J. Geophys.*, *53*, 1–15, 1983.

Collier, J. D., G. R. Helffrich, and B. J. Wood, Seismic discontinuities and subduction zones, *Phys. Earth Planet. Inter.*, *127*, 35–49, 2001.

Cormier, V. F., Slab diffraction of *S* waves, *J. Geophys. Res.*, *94*, 3006–3024, 1989.

Creager, K. C., and T. M. Boyd, Effects of earthquake mislocation on estimates of velocity structure, *Phys. Earth Planet. Sci.*, *75*, 63–76, 1992.

Creager, K. C., and T. H. Jordan, Slab penetration into the lower mantle, *J. Geophys. Res.*, *89*, 3031–3049, 1984.

Creager, K. C., and T. H. Jordan, Slab penetration into the lower mantle beneath the Mariana and other island arcs of the northwest Pacific, *J. Geophys. Res.*, *91*, 3573–3589, 1986.

Davies, D., and D. P. McKenzie, Seismic travel-time residuals and plates, *Geophys. J. R. Astron. Soc.*, *18*, 51–63, 1969.

Deal, M. M., and G. Nolet, Slab temperature and thickness from seismic tomography, 2, Izu-Bonin, Japan, and Kuril subduction zones, *J. Geophys. Res.*, *104*, 28,803–28,812, 1999.

Ding, X.-Y., and S. P. Grand, Seismic structure of the deep Kurile subduction zone, *J. Geophys. Res.*, *99*, 23,767–23,786, 1994.

Dziewonski, A. M., and D. L. Anderson, Preliminary reference Earth model, *Phys. Earth Planet. Inter.*, *25*, 297–356, 1981.

Engdahl, E. R., R. D. van der Hilst, and R. P. Buland, Global teleseismic earthquake relocation with improved travel times and procedures for depth determination, *Bull. Seismol. Soc. Am.*, *88*, 722–743, 1998.

Fischer, K. M., T. H. Jordan, and K. C. Creager, Seismic constraints on the morphology of deep slabs, *J. Geophys. Res.*, *93*, 4773–4783, 1988.

Fukao, Y., M. Obayashi, H. Inoue, and M. Nenbai, Subducting slabs stagnant in the mantle transition zone, *J. Geophys. Res.*, *97*, 4809–4822, 1992.

Gaherty, J. B., T. Lay, and J. E. Vidale, Investigation of deep slab structure using long-period *S* waves, *J. Geophys. Res.*, *96*, 16,349–16,367, 1991.

Gubbins, D., and R. Snieder, Dispersion of *P* waves in subducted lithosphere: Evidence for an eclogite layer, *J. Geophys. Res.*, *96*, 6321–6333, 1991.

Jordan, T. H., Lithospheric slab penetration into the lower mantle beneath the Sea of Okhotsk, *J. Geophys.*, *43*, 473–496, 1977.

Jordan, T. H., A. L. Lerner-Lam, and K. C. Creager, Seismic imaging of mantle convection: The evidence for deep circulation, in *Mantle Convection: Plate Tectonics and Global Dynamics*, edited by W. R. Peltier, pp. 97–201, Gordon and Breach, Newark, N. J., 1989.

Kendall, J.-M., and C. J. Thomson, Seismic modelling of subduction zones with inhomogeneity and anisotropy, I, Teleseismic *P*-wavefront tracking, *Geophys. J. Int.*, *112*, 39–66, 1993.

Koper, K. D., D. A. Weins, L. M. Dorman, J. A. Hildebrand, and S. C. Webb, Modeling the Tonga slab: Can travel time data resolve a metastable olivine wedge?, *J. Geophys. Res.*, *103*, 30,079–30,100, 1998.

Lay, T., Localized velocity anomalies in the lower mantle, *Geophys. J. R. Astron. Soc.*, *72*, 483–516, 1983.

Lay, T., The fate of descending slabs, *Annu. Rev. Earth Planet. Sci.*, *22*, 33–61, 1994.

Lay, T., *Structure and Fate of Subducting Slabs*, 185 pp., Academic, San Diego, Calif., 1997.

Mikumo, T., Source process of deep and intermediate earthquakes as inferred form long-period *P* and *S* waveforms, 2, Deep focus and intermediate depth earthquakes around Japan, *J. Phys. Earth*, *19*, 303–320, 1971.

Olson, P., P. G. Silver, and R. W. Carlson, The large-scale structure of convection in the Earth's mantle, *Nature*, *344*, 209–215, 1990.

Pankow, K. L., and T. Lay, Constraints on the Kurile slab from shear wave residual sphere analysis, *J. Geophys. Res.*, *104*, 7255–7278, 1999.

Pankow, K. L., Q. Williams, and T. Lay, Using shear wave amplitude patterns to detect metastable olivine in subducted slabs, *J. Geophys. Res.*, *107*(B6), 10.1029/2001JB000608, 2002.

Schwartz, S. Y., T. Lay, and S. L. Beck, Shear wave travel time, amplitude, and waveform analysis for earthquakes in the Kurile slab: Constraints on deep slab structure and mantle heterogeneity, *J. Geophys. Res.*, *96*, 14,445–14,460, 1991a.

Schwartz, S. Y., T. Lay, and S. P. Grand, Seismic imaging of subducted slabs: Trade-offs with deep path and near-receiver effects, *Geophys. Res. Lett.*, *18*, 1265–1268, 1991b.

Sekiguchi, S., Amplitude distribution of seismic waves for laterally heterogeneous structures including a subducting slab, *Geophys. J. Int.*, *111*, 448–464, 1992.

Silver, P. G., and W. W. Chan, Observations of body-wave multipathing from broadband seismograms: Evidence for lower-mantle slab penetration beneath the Sea of Okhotsk, *J. Geophys. Res.*, *91*, 13,787–13,802, 1986.

Silver, P. G., R. W. Carlson, and P. Olson, Deep slabs, geochemical heterogeneity, and the large-scale structure of mantle convection: Investigation of an enduring paradox, *Annu. Rev. Earth Planet. Sci.*, *16*, 477–541, 1988.

Sleep, N. H., Teleseismic *P* wave transmission through slabs, *Bull. Seismol. Soc. Am.*, *63*, 1349–1373, 1973.

Suetsugu, D., Lower mantle high-velocity zone beneath the Kurils as inferred from *P*-wave travel time and amplitude data, *J. Phys. Earth*, *37*, 265–295, 1989.

Suetsugu, D., Defocusing of teleseismic *P*-waves by the Tonga-Kermadec slab, *Geophys. Res. Lett.*, *26*, 2785–2788, 1999.

van der Hilst, R. D., and R. Snieder, High-frequency precursors to *P* wave arrivals in New Zealand: Implications for slab structure, *J. Geophys. Res.*, *101*, 8473–8488, 1996.

van der Hilst, R. D., E. R. Engdahl, W. Spakman, and G. Nolet, Tomographic imaging of subducted lithosphere below northwest Pacific island arcs, *Nature*, *353*, 37–43, 1991.

van der Hilst, R. D., E. R. Engdahl, and W. Spakman, Tomographic inversion of *P* and *pP* data for aspherical mantle structure below the northwest Pacific region, *Geophys. J. Int.*, *115*, 264–302, 1993.

van der Hilst, R. D., S. Widiyantoro, and E. R. Engdahl, Evidence for deep mantle circulation from global tomography, *Nature*, *386*, 578–584, 1997.

van der Hilst, R. D., S. Widiyantoro, K. C. Creager, and T. McSweeney, Deep subduction and aspherical variations in *P* wave speed at the base of Earth's mantle, in *Observational and Theoretical Constraints on the Core Mantle Boundary Region*, *Geodyn. Ser.*, vol. 28, edited by M. Gurnis et al., pp. 5–20, AGU, Washington, D. C., 1998.

Vidale, J. E., Waveform effects of a high-velocity, subducted slab, *Geophys. Res. Lett.*, *14*, 542–545, 1987.

Vidale, J. E., Finite-difference calculation of traveltimes in three dimensions, *Geophysics*, *55*, 521–526, 1990.

Vinnik, L. P., and R. Kind, Ellipticity of teleseismic *S*-particle motion, *Geophys. J. Int.*, *113*, 165–174, 1993.

Weber, M., Computation of body-wave seismograms in absorbing 2-D media using the Gaussian beam method: Comparison with exact methods, *Geophys. J.*, *92*, 9–24, 1988.

Weber, M., Subduction zones—Their influence on travel times and amplitudes of *P* waves, *Geophys. J. Int.*, *101*, 529–544, 1990.

Zhao, D., A. Hasegawa, and H. Kanamori, Deep structure of Japan subduction zone as derived from local, regional, and teleseismic events, *J. Geophys. Res.*, *99*, 22,313–22,329, 1994.

Zhou, H.-W., and D. L. Anderson, Search for deep slabs in the northwest Pacific mantle, *Proc. Natl. Acad. Sci. U. S. A.*, *86*, 8602–8606, 1989.

Zhou, H.-W., D. L. Anderson, and R. W. Clayton, Modeling of residual spheres for subduction zone earthquakes, 1, Apparent slab penetration signatures in the NW Pacific caused by deep diffuse mantle anomalies, *J. Geophys. Res.*, *95*, 6799–6827, 1990.

T. Lay, Earth Sciences Department, University of California, Applied Sciences Bldg, Santa Cruz, CA 95064-1077, USA. (tlay@earthsci.ucsc.edu)

K. L. Pankow, Seismograph Stations, 135 S 1460 E Rm 705, University of Utah, Salt Lake City, UT 84112-0111, USA. (pankow@seis.utah.edu)